

# Properties of the X-ray brightest Abell-type clusters of galaxies (XBACs) from ROSAT All-Sky Survey data — I. The sample

H. Ebeling<sup>1,2,\*</sup>, W. Voges<sup>1</sup>, H. Böhringer<sup>1</sup>, A.C. Edge<sup>2</sup>, J.P. Huchra<sup>3</sup>, U.G. Briel<sup>1</sup>

<sup>1</sup> Max-Planck-Institut für extraterrestrische Physik, Giessenbachstr., D-85740 Garching, Germany

<sup>2</sup> Institute of Astronomy, Madingley Road, Cambridge CB3 0HA, UK

<sup>3</sup> Harvard-Smithsonian Center for Astrophysics, 60 Garden Street, Cambridge, MA 02138, USA

\* send correspondence to [ebeling@ast.cam.ac.uk](mailto:ebeling@ast.cam.ac.uk) or [ebeling@ifa.hawaii.edu](mailto:ebeling@ifa.hawaii.edu)

Received \*\*\*; in original form 1995 September \*\*\*

## ABSTRACT

We present an essentially complete, all-sky, X-ray flux limited sample of 242 Abell clusters of galaxies (six of which are double) compiled from ROSAT All-Sky Survey data. Our sample is uncontaminated in the sense that systems featuring prominent X-ray point sources such as AGN or foreground stars have been removed. The sample is limited to high Galactic latitudes ( $|b| \geq 20^\circ$ ), the nominal redshift range of the ACO catalogue of  $z \leq 0.2$ , and X-ray fluxes above  $5.0 \times 10^{-12}$  erg cm $^{-2}$  s $^{-1}$  in the 0.1 – 2.4 keV band. Due to the X-ray flux limit, our sample consists, at intermediate and high redshifts, exclusively of very X-ray luminous clusters. Since the latter tend to be also optically rich, the sample is not affected by the optical selection effects and in particular not by the volume incompleteness known to be present in the Abell and ACO catalogues for richness class 0 and 1 clusters.

Our sample is the largest X-ray flux limited sample of galaxy clusters compiled to date and will allow investigations of unprecedented statistical quality into the properties and distribution of rich clusters in the local Universe.

**Key words:** galaxies: clustering – X-rays: galaxies – cosmology: observations – large-scale structure of Universe – surveys

## 1 INTRODUCTION

Being the largest gravitationally bound systems to have decoupled from the Hubble expansion of the Universe, clusters of galaxies are ideal tracers of the formation and evolution of structure on the largest mass scales. In the past, galaxy clusters were detected and classified mainly on the grounds of their optical appearance, the largest compilations of this kind being the catalogues of Abell (1958), Abell, Corwin & Olowin (1989, from here on ACO), and Zwicky and co-workers (1961–1968). In particular the Abell and ACO catalogues have been used extensively for statistical studies of cluster properties, but served also as finding lists for more detailed investigations of individual clusters.

The major drawback of optical compilations of this kind lies in the high risk of projection effects corrupting the sample. Since the cluster detection and selection is performed on the two-dimensional distribution of galaxies as it appears in projection on optical plates, fluctuations in the surface density of field galaxies as well as superpositions of poor clusters along the line of sight can lead to an overestimation of a system's richness. On the other hand, poor clusters can be missed completely as they often do not contrast strongly with the background field. Several studies have investigated the statistical completeness and contamination of the Abell catalogue

emphasizing the importance of projection effects for optically selected cluster samples (Lucey 1983, Sutherland 1988, Struble & Rood 1991).

The serious problem of projection effects can, however, be overcome completely by selecting clusters in the X-ray rather than in the optical. X-ray emission from a diffuse, gaseous intra-cluster medium (ICM) trapped and heated to temperatures of typically a few  $10^7$  K is not only a sure indication that the system is indeed three-dimensionally bound. Being caused by ion-ion collisions in the ICM, the X-ray flux is proportional to the square of the ion density and thus much more peaked at the gravitational centre of the cluster than the projected galaxy distribution. This property requires clusters to be almost perfectly aligned along the line of sight in order to be mistaken for a single, more luminous entity, so that projection effects caused by such superpositions can be effectively neglected in the X-ray.

X-rays thus provide a very efficient and unbiased way of compiling cluster samples which, as far as statistical studies are concerned, will eventually supersede the present, optical catalogues. Early statistical cluster samples have been compiled from the X-ray data taken by the UHURU (Schwartz 1978), ARIEL V (McHardy 1978), and HEAO 1 A-2 satellites (Piccinotti et al. 1982), all of

which comprised about 30 clusters. Including clusters detected during the EXOSAT mission, Lahav et al. (1989) and Edge et al. (1990) presented an X-ray flux limited sample of 55 clusters, very similar in size to that compiled by Gioia et al. (1990) from X-ray sources detected in the EINSTEIN Medium Sensitivity Survey. Projects aimed at the compilation of purely X-ray selected cluster samples based on the X-ray data collected during the ROSAT All-Sky Survey (RASS, Voges 1992) are well under way in both the northern (Allen et al. 1992, Giacconi & Burg 1993, Crawford et al. 1995) and the southern hemisphere (Guzzo et al. 1995, De Grandi 1996, see also Pierre et al. 1994); the two-point correlation function for RASS selected cluster samples compiled in smaller sky areas has been presented recently (Nichol et al. 1994, Romer et al. 1994) showing again the advantage of X-ray over optical selection procedures. An overview of the various RASS cluster projects is given in Böhringer (1994).

In the following, we shall pursue an approach that investigates the X-ray properties of optically selected clusters and leads to an all-sky sample of the X-ray brightest Abell-type clusters of galaxies (XBACs)\* which is more than four times larger than the largest X-ray flux limited cluster sample published to date.

In this first article of a series we present the sample and discuss its statistical properties; in subsequent papers we shall establish the X-ray luminosity function of Abell-type clusters of galaxies (Ebeling et al., in preparation) as well as the cluster-cluster correlation function (Edge et al., in preparation), and investigate correlations between X-ray and optical properties of the XBACs.

Throughout this paper, we assume an Einstein-de Sitter Universe with  $q_0 = 0.5$  and  $H_0 = 50 \text{ km s}^{-1} \text{ Mpc}^{-1}$ .

## 2 THE OPTICAL DATABASE

All optical Abell cluster parameters used here, including the cluster coordinates, are taken from ACO's 1989 publication. Of the original 4076 clusters in the catalogue, we discard A 3541 and A 3897 as secondary detections of A 1664 and A 2462, respectively.

Besides the actual cluster coordinates the most crucial cluster parameter for both the compilation of our sample and the subsequent analysis of various physical cluster properties is possibly the cluster's redshift. Although the number of measured redshifts for Abell and ACO clusters of galaxies has seen an impressive increase in the past decade, we still have to rely on estimated redshifts for the large majority of the more distant clusters. In the following paragraphs we shall describe briefly the procedure adopted by us for the estimation of redshifts for ACO clusters without, or with questionable, measured redshifts.

Attempts to estimate redshifts from different optical parameters, such as  $m_1$ ,  $m_3$ ,  $m_{10}$ , the apparent cluster diameter or a combination of any of these, have been described by various authors (Abell 1958, Corwin 1974, Leir & van den Bergh 1977, Postman et al. 1985, ACO, Couchman et al. 1989, Scaramella et al. 1991, Peacock & West 1992). Our calibration relies on the most commonly used redshift estimator,  $m_{10}$ , which is statistically more robust than  $m_1$  or  $m_3$  and has the additional advantage of being available for all of the catalogued clusters.

The  $m_{10}-z$  relation used in the following to obtain distance

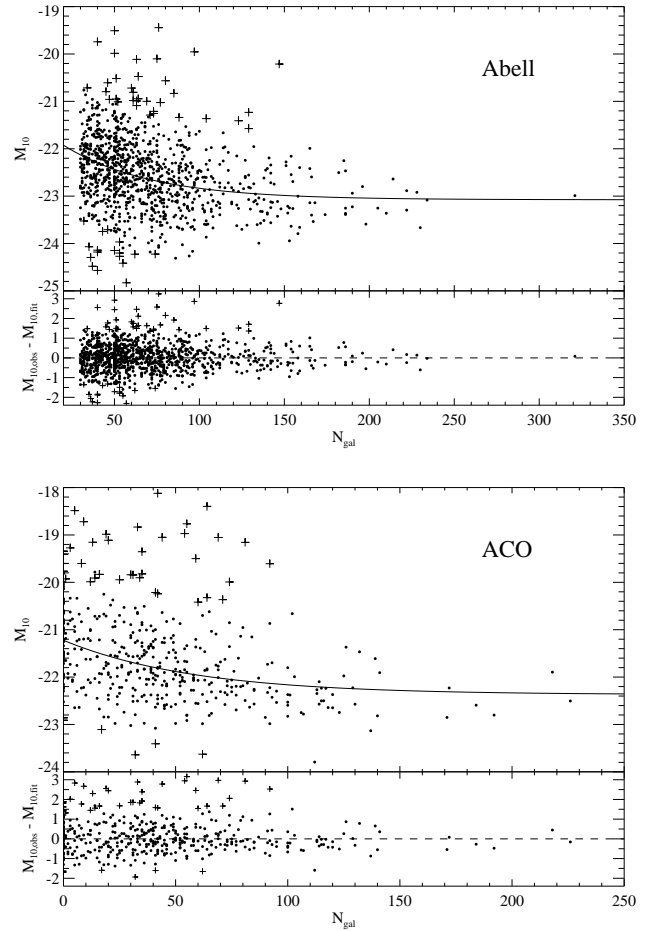


**Figure 1.** The richness dependence of  $M_{10}$ , the Scott effect, for Abell and ACO clusters. For each sample the least-squares fit of a constant plus an exponential is overlaid; the bottom panels show the respective residuals. Clusters marked by crosses are those discarded as inconsistent with the  $m_{10}-z$  relation.

estimates for those clusters which do not have measured  $z$ 's is calibrated with 1482 Abell and ACO clusters with known redshifts (including 182 southern supplementary ACO clusters), the great majority of which have been compiled by one of us (JPH). Additional ACO cluster redshifts are taken from Heinz Andernach's compilation (Andernach 1991) and the NASA Extragalactic Database NED. Also, we are indebted to C.A. Collins, A.K. Romer, C.S. Crawford and G.B. Dalton for allowing us to use, prior to publication, some of the redshifts taken by them for different projects. As for the cluster redshifts obtained in the APM redshift survey, we use the Abell identifications and redshifts given by Ebeling & Maddox (1995) rather than those published by Dalton et al. (1994).

Note that, although we do take the ACO supplementary clusters into account for the purpose of the  $m_{10}-z$  calibration, we do not consider them in the rest of this paper.

For the actual calibration, the 'raw'  $m_{10}$  values in the respective photometric system (R in the north, V in the south) are corrected only for Galactic extinction. In the north, the values listed by Abell can thus be used straight away, whereas in the south ACO's V magnitudes are corrected for Galactic extinction following the procedure described by Fisher & Tully (1981).

The K-correction is taken to be  $K(z) = 1.122 z$  for the north-

\* An early, if incomplete, version of this sample has been presented by Ebeling (1993).

	$c_0$	$c_1$	$c_2$
north	-23.08	1.70	-0.020
south	-22.37	1.15	-0.017

**Table 1.** The final values for the Scott–effect coefficients of Eq. 1 obtained in least-squares fits to the richness- $M_{10}$  distributions of Abell clusters (north) and ACO clusters (south).

ern red plates (Postman et al. 1985) and  $K(z) = 4.14 z - 0.44 z^2$  for the southern IIIa-J plates<sup>†</sup> (Ellis 1983). For the K-corrected magnitudes the correction for the Scott effect (Scott 1957) is then determined from the dependence of the absolute magnitude of the tenth brightest cluster galaxy,  $M_{10}$ , on the cluster richness as given by the Abell number of galaxies,  $n_{\text{gal}}$ . We model the Scott effect as an exponential plus a constant,

$$M_{10}(n_{\text{gal}}) = c_0 + c_1 \exp(c_2 n_{\text{gal}}), \quad (1)$$

where the coefficients  $c_i$  are obtained in separate fits to the data in the northern and southern hemisphere. The correction term is then given by  $\Delta M_{10,\text{Scott}} = M_{10}(n_{\text{gal}}) - M_{10}(50)$ , i.e., a nominal richness of  $n_{\text{gal}} = 50$  is used as a reference point. Applying the corrections for both reddening and the Scott effect then yields a tentative  $m_{10}$ - $z$  relation which we take to be of the simple form  $\log_{10} z_{\text{est}} = a + b m_{10}$ . The final coefficients  $c_i$  (listed in Table 1) as well as  $a$  and  $b$  are determined in an iteration loop where redshifts with  $(z_{\text{obs}} - z_{\text{est}})/z_{\text{obs}} \geq 3\sigma$  or  $(z_{\text{obs}} - z_{\text{est}})/z_{\text{est}} \geq 3\sigma$  are progressively removed. This approach leads to the exclusion of 52 northern Abell clusters (leaving 984) and 48 southern ACO main and supplementary clusters (leaving 398) from the calibration.

Figures 1 to 3 show the resulting distributions for Abell and ACO clusters as well as the residuals from the respective least-squares fits.

The  $m_{10}$ - $z$  relation finally adopted by us is then given by

$$\begin{aligned} \log z_{\text{est}} &= (-4.50 \pm 0.56) + (0.212 \pm 0.033) \times \\ &\quad (m_{10} - \Delta M_{10,\text{Scott}} - K(z_{\text{est}})) \\ &\quad \text{Abell clusters} \\ &= (-4.24 \pm 0.66) + (0.190 \pm 0.041) \times \\ &\quad (m_{10} - \Delta M_{10,\text{Scott}} - K(z_{\text{est}})) \\ &\quad \text{ACO clusters} \end{aligned}$$

Note, firstly, that, just as in the calibration where the cluster redshifts are known from measurements, the K-correction is computed iteratively at the *estimated* redshift, and, secondly, that for both samples the slope of the linear calibration is in good agreement with the theoretically expected value of 0.2.

For Abell clusters the  $m_{10}$ - $z$  relation thus obtained is consistent with the findings of Postman et al. (1985) but has a lower dispersion of  $\sigma(\log z - \log z_{\text{est}}) = 0.11$  (compared to 0.14). For the southern ACO main and supplementary clusters we find the same value of  $\sigma(\log z - \log z_{\text{est}}) = 0.11$ . In both cases the above mentioned  $3\sigma$  outliers have been ignored.

Figure 4 finally shows the resulting redshift distribution for

<sup>†</sup> Strictly speaking, these K-corrections are valid only for elliptical and S0 galaxies; assuming that the tenth brightest galaxy is of that type does not introduce a big error, however, as spirals are rare among the bright galaxies in rich clusters.

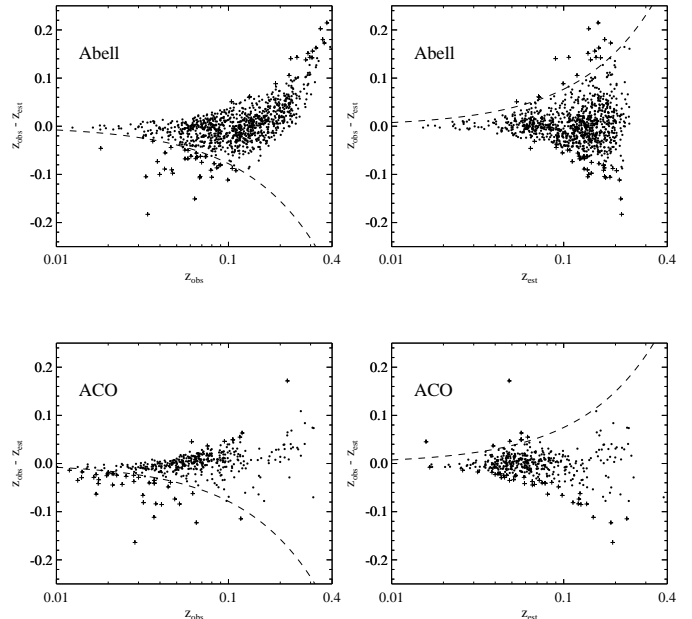


**Figure 2.** The difference between measured and estimated redshifts as a function of  $z$  and  $m_{10}$ , respectively, for Abell and ACO clusters. For each sample the  $3\sigma$  limits from the  $m_{10}$ - $z$  relation are overlaid as dashed lines. Clusters marked by crosses are those discarded as inconsistent with the  $m_{10}$ - $z$  relation.

Abell and ACO clusters. We should like to emphasize once more that the southern supplementary clusters have been included only temporarily for the purpose of our  $m_{10}$ - $z$  calibration but are not included in the ACO sample as we use it here and in the following. Also, the measured redshifts of clusters excluded from the  $m_{10}$ - $z$  calibration because of inconsistencies between the measured and estimated redshifts are not necessarily rejected as interlopers, but scrutinized and only replaced by estimates if the measured redshift is based on a single galaxy redshift that is clearly in the foreground of the actual cluster. Having replaced 22 northern and 30 southern cluster redshifts with estimates, we are left with measured (and credible) redshifts for 1014 clusters from Abell's original compilation and 246 southern ACO clusters.

### 3 THE X-RAY DATABASE

From August 1990 to February 1991, the ROSAT X-ray satellite conducted an all-sky survey (RASS) in the soft X-ray energy band ranging from 0.1 to 2.4 keV. Overviews of the ROSAT mission in general and the RASS in particular can be found in the literature (Trümper 1993, Voges 1992). A first processing of the data taken by the Position Sensitive Proportional Counter (PSPC, Pfeffermann et al. 1986) during the RASS was performed as the survey proceeded using the Standard Analysis Software System (SASS) developed for this purpose (Voges et al. 1992) at MPE. To this end, the incoming X-ray data were sorted into two-degree wide strips of constant ecliptic longitude following the satellite's scanning motion on the sky. Only two days worth of data are collected in one strip, though, so that the exposure time in each strip is roughly constant at some 360 s, and the much longer exposure times accumulated around the ecliptic poles are not taken advantage of.

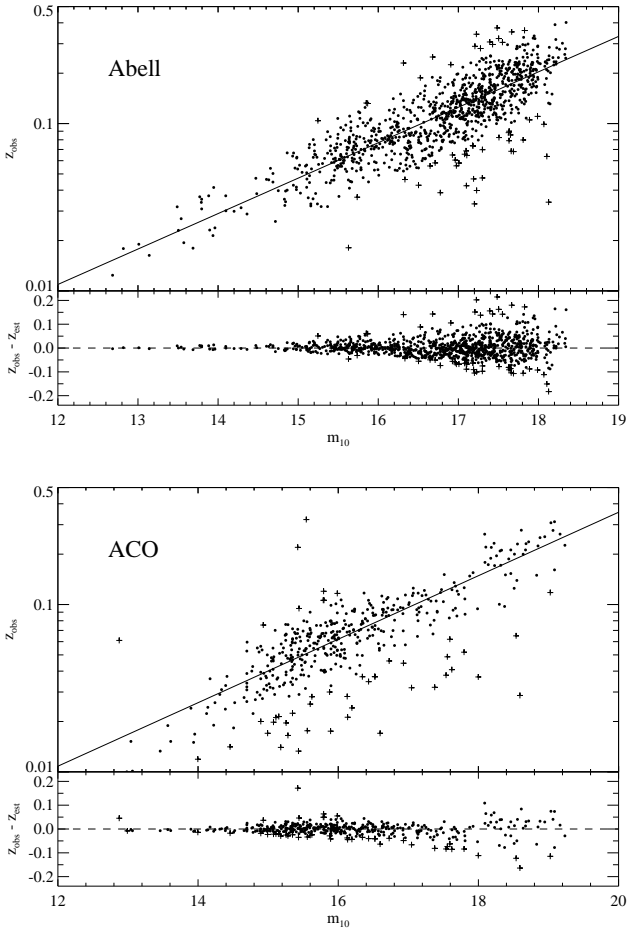


**Figure 3.** The Hubble diagrams for 984 Abell and 398 ACO main and supplementary clusters. The solid lines represent the least-squares fits to the data; for each sample the bottom panel shows the respective residuals on a linear scale. Clusters marked by crosses are those discarded as inconsistent with the  $m_{10}$ - $z$  relation.

Running on the ninety strips representing the RASS in this framework, the SASS detected 49 441 X-ray sources (multiple detections removed) which constitute the X-ray sample most of the statistical RASS studies performed to date are based upon. The source count distribution for all 49 441 SASS sources from this master source list is depicted in Fig. 5 and shows that a minimum of some 10 photons is required for any source in order to be detected reliably in this first processing of the RASS data.

Since 1992 so-called PET files (for Photon Event Table) are produced at MPE, which contain the full photon information in a field of specified size around any given position in the sky thereby overcoming the limitations of the strip data used in the earlier processing.

#### 4 A TENTATIVE SAMPLE

Starting from the results of the first SASS processing mentioned above, we select a subset of 10 241 sources with SASS count rates in excess of  $0.1 \text{ s}^{-1}$ . This threshold is the result of a compromise between maximal sky coverage and maximal survey depth: for sources consisting of less than 13 photons the SASS source list

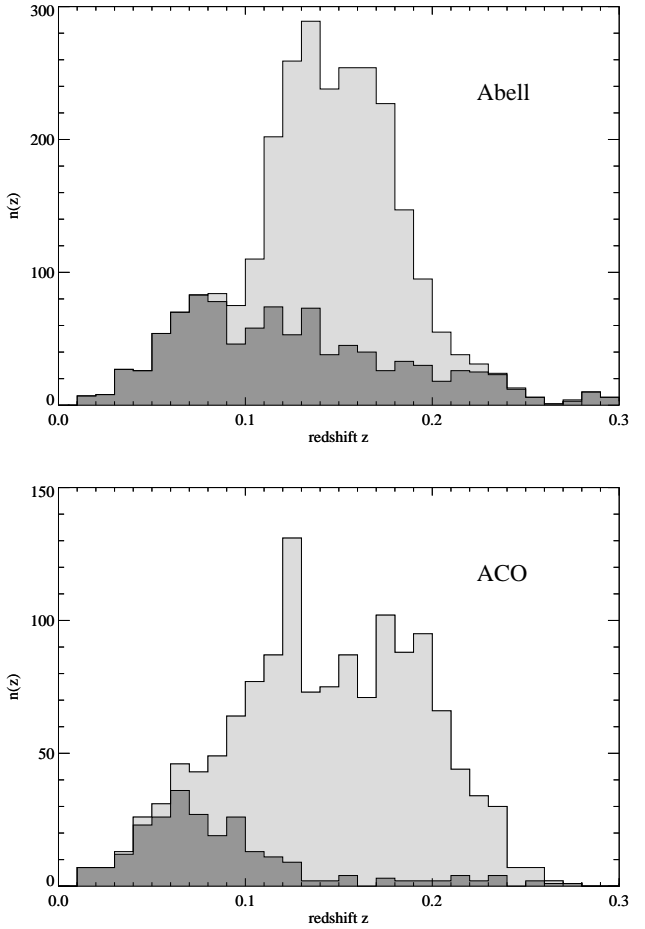


**Figure 4.** The redshift distribution of Abell and ACO clusters of galaxies combining measured (dark shading) and estimated values (light shading)

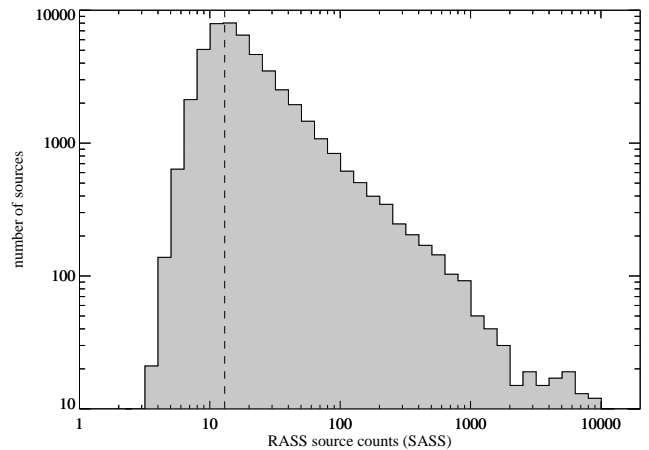


**Figure 5.** The differential frequency distribution of the X-ray photon counts in RASS sources as detected by the SASS. Accordingly, the SASS master source list starts to become incomplete at source strengths of about 13 photons.

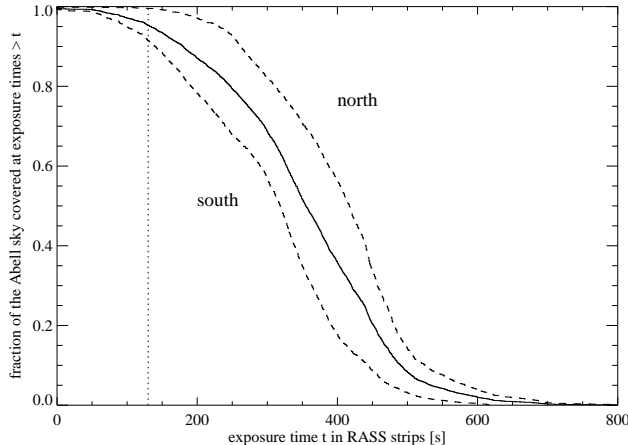


**Figure 6.** The cumulative frequency distribution of the RASS exposure times in the strips the first SASS processing was performed on. Exposure times are computed in squares of 23 arcmin<sup>2</sup> area around the nominal positions of the 4074 catalogued ACO clusters. If a position falls into more than one strip, the highest exposure time is used.

starts to become incomplete (see Fig. 5), and at minimal exposure times higher than 130 seconds the sky coverage of the RASS at the positions of ACO clusters starts to fall below 95 per cent. The latter figure is derived from the distribution shown in Fig. 6. Note that in the southern hemisphere the completeness with respect to Abell sky coverage is only 91.6 per cent as opposed to 99.6 per cent in the north, due to the fact that, in order to avoid damage to the detector, the PSPC is switched off automatically when passing through regions of enhanced particle background, for instance around the so-called South-Atlantic Anomaly.

We cross-correlate the reduced SASS X-ray source list with the ACO cluster catalogue using the clusters' redshifts to scale angular to metric separations. Estimated redshifts based on  $m_{10}$  and taking into account the cluster richness are used where measured redshifts are not available (see Section 2). Figure 7 shows the resulting cumulative distribution of the separations between the SASS X-ray sources' and the optical cluster positions in units of Abell radii ( $r_A$ ). A parabolic contribution from random coincidences fitted to the data in the  $0.75 \leq r/r_A \leq 1.5$  range has been subtracted (the dash-dotted curve in Fig. 7). The total number of true coincidences of 510 is indicated by the dashed line in Fig. 7.

We extract a 95 per cent complete sample by selecting the 547 correlation pairs (corresponding to 480 clusters) found out to respective separations of 0.407 Abell radii. As even at  $z = 0.4$  this cutoff still translates into an angular separation of more than 3 arcmin, it is always larger than the uncertainty in the optical cluster positions of typically 2 to 3 arcmin (ACO) which therefore do not need to be taken into account separately. Some 62 entries from this list, i.e. 11 per cent, can be expected to be coincidental.

Of the 121 catalogued ACO clusters with  $z \leq 0.05$  only 60 are contained in this list. The lack of SASS detections in excess of  $0.1 \text{ s}^{-1}$  for the remaining 61 nearby ACO clusters is, however, not necessarily indicative of their being intrinsically X-ray faint. Rather, it is possible that the SASS detection algorithms have underestimated the flux from such potentially highly extended sources or may have missed the source altogether, as the SASS was designed solely for the detection of point sources. We therefore also include the re-

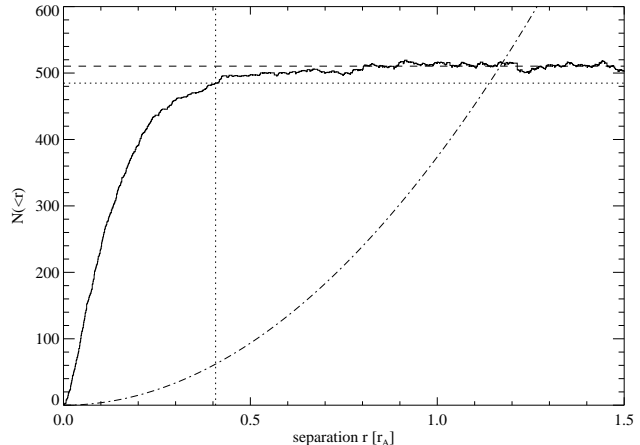


**Figure 7.** The cumulative number of coincidences in the cross-correlation between the ACO catalogue and the RASS X-ray source list provided by the SASS as a function of the X-ray to optical source separation in Abell radii ( $r_A$ ). A parabolic background component (the dot-dashed line) has been subtracted.

maining 61 ACO clusters with  $z \leq 0.05$  which brings the total number of ACO clusters in our tentative sample to 541.

For 535 of these, we obtained PET data in  $2 \times 2 \text{ deg}^2$  fields around the optical cluster position. As the PET file for any field contains all photons accumulated during the whole RASS in the respective region, the accumulated exposure times in these fields are higher than those available in the SASS strips; up to 5800 s are attained. As mentioned before, the SASS has difficulties characterizing or, for that matter, even reliably detecting extended emission. The cause for this lies in the algorithm's basic design as a point detection algorithm which is primarily sensitive to local and quasi-spherical intensity variations. We therefore re-processed the RASS data in the 535 fields with VTP (for Voronoi Tesselation & Percolation), an algorithm developed for the detection and characterization of sources of essentially arbitrary shape (Ebeling & Wiedenmann 1993, Ebeling 1993). VTP works on the individual photons rather than on spatially binned representations of the data; also it does not require any model profiles to be fitted to the detected emission in order to determine fluxes all of which makes the algorithm extremely versatile and flexible. The reprocessing of the data with VTP is crucial in order to obtain reliable fluxes for the clusters in our sample: for clusters of galaxies, raw SASS fluxes are found to be typically too low by about a factor of 0.5; for nearby clusters the misassessment can even exceed one order of magnitude (cf. Section 10.1; see also Ebeling 1993).

Of the six potential cluster detections for which no PET files are available, two can in fact be identified with stars whose positions agree within a few arcsecs with those of the respective SASS source. A third candidate features a spectral hardness ratio (see below) of  $-0.26$  and is also clearly off the cluster core as seen on the optical plates, so that we can safely discard it as a non-cluster source. Of the remaining three possible cluster detections, two (A 295 and A 3089) were not detected by SASS at count rates greater than  $0.1 \text{ s}^{-1}$  and came in only because of their low redshift; in fact A 3089 is not detected by the SASS at any flux limit. Excluding A 3089, we are left with two detections, the second of which (A 3899) features an X-ray to optical separation of  $0.4 r_A$  and, accordingly, has a very high probability of in fact being a chance coincidence. We conclude that of the six clusters for which PET data

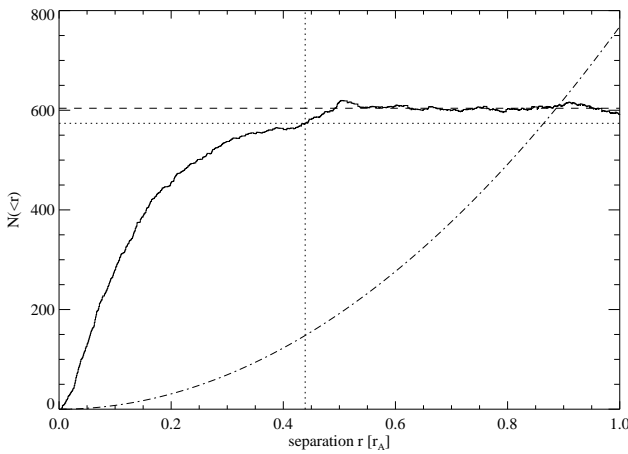


**Figure 9.** The cumulative number of coincidences in the cross-correlation between the ACO catalogue and the RASS X-ray source list provided by VTP as a function of the X-ray to optical source separation. A parabolic background component (the dot-dashed line) has been subtracted.

are not available for a VTP re-analysis at most two, namely A 295 and A 3899, may qualify for inclusion in the XBACs sample.

The 3498 sources detected by VTP in the 535 PET fields were then screened for possible blends of close source pairs. 228 potential blends were visually inspected, and in 45 cases blended sources were separated by introducing a dividing line into the field. Figure 8 illustrates the problem of VTP-produced blends by showing the raw photon distribution and the VTP sources detected around A 2201.

Subsequently, the merged VTP X-ray source list for all PET fields was correlated against the ACO catalogue, and, just as before, a 95 per cent complete sample of coincidences was compiled (see Fig. 9). The maximal separation between the included matches is 0.439 Abell radii. This sample now comprises 723 X-ray sources corresponding to 599 ACO clusters, the higher number being due to additional VTP detections of nearby clusters missed or misassessed by the SASS, and also to a number of serendipitous detections of X-ray faint ACO clusters in the selected PET fields.

## 5 REMOVAL OF NON-CLUSTER SOURCES

Clearly, this sample cannot be used as it stands, as, statistically, about 148 (i.e. some 21 per cent) of its entries are caused by random coincidences between the optical ACO cluster positions and non-cluster X-ray sources. In fact this figure is still a lower limit since, in addition to truly random coincidences, we also expect a few percent of the listed matches to be with non-cluster sources like QSOs or AGN which are, however, cluster members. In order to identify chance coincidences as well as cluster-related point sources, we searched the SIMBAD database in Strasbourg for alternative optical counterparts for the 723 VTP-detected X-ray sources. For each X-ray source, we also obtained  $12' \times 12'$  optical images from the POSS and UK Schmidt sky surveys through the extremely useful SKYVIEW facility<sup>‡</sup> and looked for possible optical identifications. Also, we searched the ROSAT public archive of pointed PSPC and HRI observations for further X-ray data for our cluster

candidates. The 135 deeper X-ray images thus obtained plus another seven from non-public pointed observations awarded to members of the IoA X-ray group were then examined in order to ensure that the emission detected by VTP in the RASS data originates indeed from the ICM. The pointed observations were also used to obtain X-ray fluxes to be used as a control sample for the VTP-derived RASS fluxes (see Section 6.1).

As a result of the analysis of all these data,

- 27 of our X-ray sources are identified with stars,
- 30 turn out to be individual galaxies, AGN, or QSOs, and
- four are groups or distant clusters of galaxies that are close to but clearly not related to the Abell clusters they have been associated with.
- In 45 cases, the X-ray source cannot be assigned unambiguously to an optical counterpart, but is point-like and not associated with any enhancement in the projected galaxy density, which is why we reject these sources too as unrelated.
- For 18 clusters, the detected emission is heavily contaminated by point sources which may or may not be related to the cluster. We make no attempt at disentangling the clusters' and the contaminants' contribution, and discard these candidates, for all of which the diffuse emission is negligible in comparison to the dominating point source.
- Finally, we eliminate another 41 X-ray sources, most of which are very faint, on the grounds of their being either spurious or not fully contained in the respective PET field. Some of the latter are also (and wholly) contained in a neighbouring field so that in these cases the clusters concerned are actually not lost from the sample.

In Table 2 we list the 37 sources that could be bright enough to get included in our flux limited sample (see Section 7 for a discussion of the XBACs' flux limit of completeness) but were discarded as non-cluster sources in the above procedure. Note that our assessment of these sources' brightness is based on their count rates only, as a rigorous conversion to X-ray fluxes requires knowledge of the physical emission process.

In the course of the visual inspection of both the X-ray and the optical images of all our candidate sources we also encountered a few cases where extended X-ray emission clearly detected in the RASS data is missing from our tentative list as the respective source is too far away from the nominal optical cluster position. After careful examination of the optical and X-ray data we include eight sources (associated with seven ACO clusters) at X-ray/optical separations of more than 0.439 Abell radii into our sample. Five of the affected clusters (A 548 [twice], A 1750, A 1758, A 1631, and A 3528) already had X-ray sources assigned to them in our list and thus join the small sample of double clusters (for A 625, A 901, A 2197, and A 2572 both components are already contained in our list) with both X-ray detections being of comparable brightness in all cases. For the other two (A 2537 and A 3869) the added detection is the only one, and, in particular in the case of A 3869, it is not entirely clear whether the system detected by ACO in the optical is in fact the same as the cluster now detected in the X-ray.

So far, we have removed 165 sources from our sample on the grounds of their combined X-ray/optical appearance. A further criterion that has not yet been applied is the spectral hardness of the X-ray emission. We use the SASS definition of a source's hardness ratio HR

$$HR = \frac{h - s}{h + s}$$

where  $h$  are the photon counts in the hard energy range from 0.5 to

<sup>‡</sup> <http://skview.gsfc.nasa.gov/skyview.html>

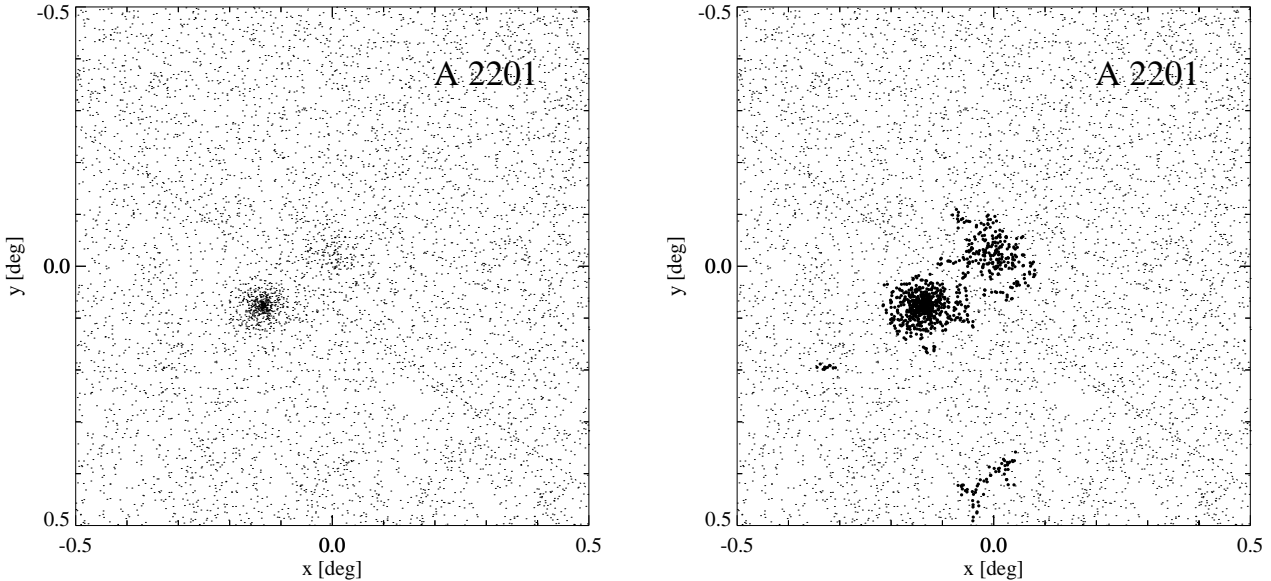


**Figure 8.** A 2201 as an example of a blended source. The plot on the left shows the photon distribution in the centre of the respective field; in the plot on the right the photons constituting the VTP sources are overlaid as bold dots. The dotted lines indicate where VTP's percolation was forced to stop in order to keep the two sources separated. The blended sources are A 2201 in the field centre and, some 10 arcmins south-east, the quasar PG 1626+554.

2 keV, and  $s$  those in the softer 0.1 to 0.4 keV band. X-ray emission from a plasma at temperatures of typically  $10^{7-8}$  K occurs predominantly in the hard band; accordingly, the hardness ratios of RASS-detected clusters of galaxies are found to be positive in more than 90 per cent of the cases (Ebeling et al. 1993). Although clusters of galaxies are intrinsically hard X-ray sources, the emitted spectrum is subject to modification on its way to the observer through absorption of soft X-rays by neutral Hydrogen in the Galaxy. The variation of the hardness ratio values observed for the 566 sources remaining in our sample with the column density of neutral Hydrogen  $n_H$  along the line of sight is shown in Fig. 10. (The  $n_H$  values are taken from the compilation of Stark et al. (1992) for declinations north of  $-40$  degrees and from Dickey & Lockman (1990) in the remainder of the sky.) As can be seen from Fig. 10, the observed HR for ICM emission can become small and even negative where the absorption is extremely low. Figure 11 shows the same distribution of HR values as a histogram; note the low-HR tail of the distribution. Some sources, (marked by open circles in Fig. 10 and light shading in Fig. 11) feature HR values much lower than what would be expected from the corresponding column density, and are thus unlikely to be due to X-ray emission from galaxy clusters. For most of the 13 soft sources highlighted in Fig. 10 the errors in the hardness ratios are, however, too large to firmly rule out a cluster origin which is why we scrutinize all 13 once more in both the X-ray and the optical. As a result,

- we exclude one source on the grounds of its X-ray spectrum being too soft to be attributed to ICM emission ( $6\sigma$  off the overall  $n_H$ -HR relation) and
- discard another seven point-like sources that can tentatively be identified as stars or AGN.

Altogether, we have thus eliminated 173 X-ray sources from our tentative sample and added in another eight which leaves us with 558 sources. Fig. 12 shows the spatial distribution of the rejected sources with respect to the nominal ACO cluster positions

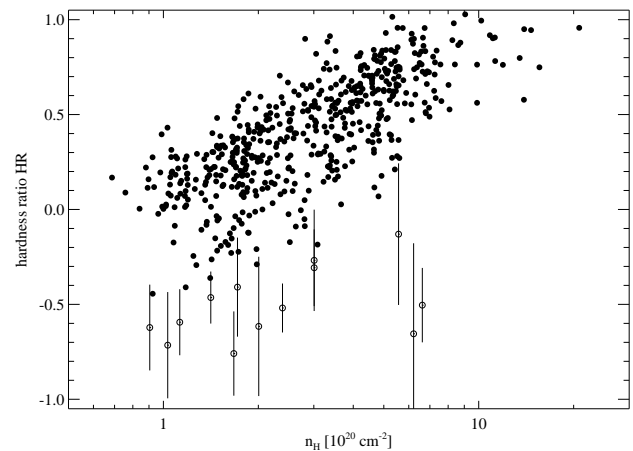


**Figure 10.** The observed spectral hardness ratio for the 566 X-ray sources of the decontaminated sample as a function of the Galactic column density of neutral Hydrogen. Open circles with error bars represent the 13 sources examined once more because of their softness.

and compares it to the same distribution for the sources remaining in the sample. Just as expected for a sample dominated by random coincidences, the removed sources' distribution is homogeneous, whereas the distribution of the sources attributed to ICM emission is found to be strongly peaked around the optical cluster position.

The 558 X-ray sources remaining in the cleaned sample are associated with 532 different ACO clusters (nine of them double), as 48 sources are classified as multiple detections of the same cluster in the sense that the extended cluster emission got picked up in more than one piece. However, contrary to the nine double clusters, the 22 clusters affected do not consist of clearly distinct subentities, which is why, for each of these 22, we merge the different sources detected by VTP into one. Accordingly, the number of X-

associated ACO cluster	$\alpha$ (J2000) [deg]	$\delta$ (J2000) [deg]	identification	comments
A2751	4.1560	-31.4213	ambiguous	probable blend of (X-ray faint) cluster and AGN
A27	6.3199	-20.8596	probable AGN	isolated galaxy is most probable id
A2807	10.1788	-34.6677	AGN	Seyfert 1, $z=0.199$ , Cristiani et al. (1995)
A2836	13.2024	-47.6170	probable AGN	on isolated galaxy
A151	17.2066	-15.6297	star	HD6853, G5, 10.1 mag
A2881	18.1192	-17.0151	star	YZ CET, 12.0 mag dMe star
A2904	20.5826	-29.2490	ambiguous	probably blend of two stars
A195	21.5654	19.1654	star	HD8723, F0, 5.3 mag
A195	21.8822	19.1838	AGN	MRK 0359, Seyfert 1.5, $v = 5007 \text{ km s}^{-1}$
A195	21.9834	18.9909	star	BD+18 193, F8, 9.2 mag
A271	28.4562	1.8797	anon star	13 mag star most probable id
A347	36.4376	41.9761	ambiguous	NGC911, $v = 5604 \text{ km s}^{-1}$ or HD14933, A0, 9.2 mag
A3107	48.7204	-42.6777	AGN	0313-428, Seyfert 1, $z=0.126$ , Monk et al. (1988)
A484	63.8387	-7.6486	star	HD 26965, K1, 4.4 mag
A3367	87.3101	-24.4209	probable AGN	IRAS 05472-2426 in error box, no published redshift
A3389	95.7874	-64.6040	AGN	Seyfert 1, IRAS C06229-6434, $z=0.130$
A3392	96.7710	-35.4898	radio galaxy	PKS0625-35, $z = 0.05459$ , core-dominated dominated central galaxy
A3408	107.1714	-49.5434	AGN	4U 0708-49, Seyfert 1, $z = 0.0411$
A689	129.3556	14.9830	prob BLLac	on flat-spectrum radio source in cluster core, Crawford et al. (1995)
A757	138.3565	47.6871	probable AGN	blend of two AGN candidates
A1030	157.7444	31.0550	AGN	B2 1028+31.3, $z = 0.1782$ , at very core of cluster
A1225	170.2863	53.8547	probable AGN	on isolated blue galaxy
A3494	179.2058	-32.2318	star	HD103743, G0, 7.0 mag
A1593	190.5454	33.2872	AGN	WAS 61, Seyfert 1, $z = 0.0439$
A1599	190.7622	2.7423	Galaxy	NGC 4636, $v = 1095 \text{ km s}^{-1}$
A3565	203.9744	-34.2951	AGN	MCG-06-30-015, Seyfert 1, $v = 2248 \text{ km s}^{-1}$
A1774	205.2705	39.9931	probable BLLac	B3 1338+402, on flat spectrum radio source in cluster core
A3574	207.3311	-30.3166	AGN	IC 4329A, Seyfert 1, $v = 4813 \text{ km s}^{-1}$
A1855	211.2495	47.1144	AGN	RX J14050+4707, $z=0.1510$ Bade et al. (1995)
A2034	227.6707	33.5958	probable AGN	on isolated galaxy
A2147	240.9162	15.9002	AGN	B1601+1602, $z=0.1095$
A3698	308.6135	-25.5439	star	PPM 736274, 9.7 mag
A3747	317.0595	-43.8522	AGN	Seyfert 1, C08.02, no published redshift, Maza et al. (1992)
A2351	323.5352	-13.4789	star	HD 205249, G5, 8.0 mag
A3915	341.6812	-52.1109	probable AGN	on isolated galaxy
A2660	356.2095	-26.0307	probable AGN	on faint blue, stellar object
A4038	357.2267	-28.1217	star	HD 223352, A0, 4.6 mag

**Table 2.** Sources with VTP count rates higher than  $0.25 \text{ s}^{-1}$  that were excluded as being dominated by, if not entirely due to, X-ray emission of non-cluster origin. The quoted positions are the centroids of the VTP detections.

ray sources drops by 26 to equal the number of unique ACO clusters, 532.

As can be seen from Figs. 10 and 11, the sample of 558 still contains a number of X-ray sources that are suspiciously soft. For many of these, but also for a number of spectrally hard sources, the X-ray images from the RASS show evidence of contamination from point sources. We flag a total of 21 clusters for which the level of contamination might exceed 30 percent of the total flux. For four of these 21, pointed data are available which will be used in Section 6.2 to quantify the contribution of point sources to the total source flux.

## 6 GETTING THE FLUXES RIGHT

Besides selection effects, the main concern when compiling an X-ray flux limited sample is the reliability and accuracy of the flux determination procedure. This section details how diffuse emission that has escaped direct detection is taken into account, compares the resulting RASS-VTP count rates with results obtained from pointed

observations, and finally describes the conversion of count rates into energy fluxes.

### 6.1 Correction for ‘missing flux’

In the presence of background radiation, the emission directly detectable by any source detection algorithm is always limited to some fraction of the total flux. The raw VTP count rates for the 523 clusters of our sample (532 if the two components of our nine double clusters are counted separately) thus have to be corrected for the low surface brightness emission in the far wings of the source that has not been detected directly. In doing this, we use King’s approximation to the density profile of an isothermal sphere (King 1962) and assume a source profile of the form

$$\sigma_K(r) = \sigma_0 [1 + (r/r_c)^2]^{-3\beta+1/2} \equiv \sigma_0 \tilde{\sigma}_K(r) \quad (2)$$

(Cavaliere & Fusco-Femiano 1976) where  $\sigma_K(r)$  is the projected surface brightness as a function of radius. Fixing the beta parameter at a value of 2/3 (Jones & Forman 1984), we can derive both

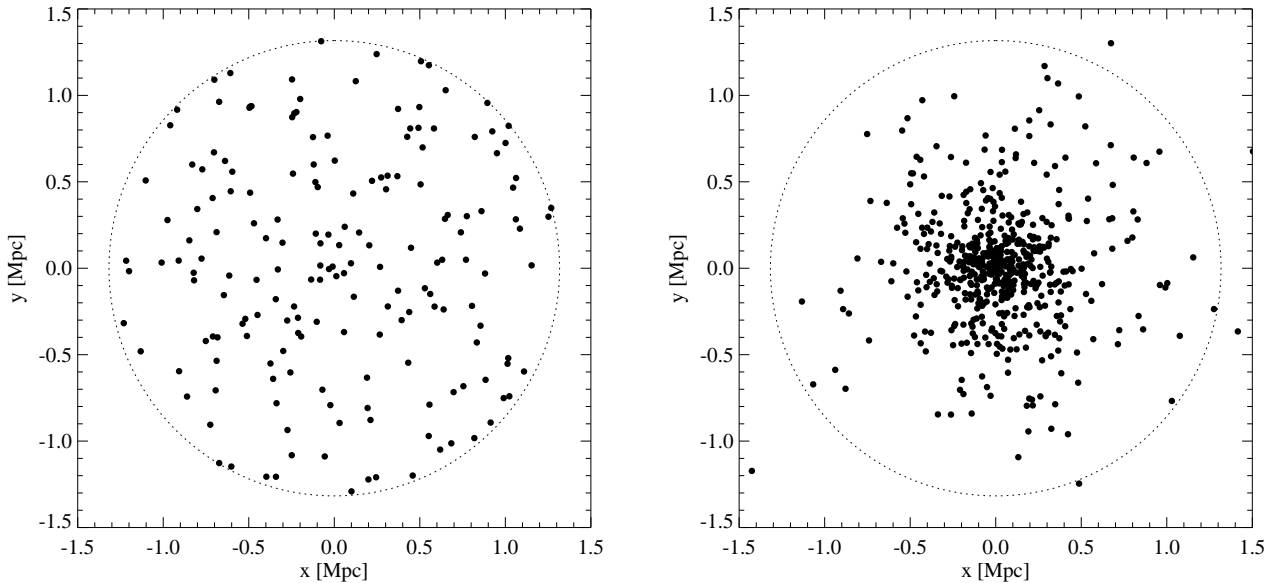


**Figure 12.** The projected spatial distribution of the 173 X-ray sources removed from the sample around the nominal cluster positions (left) and the same distribution for the 558 sources accepted as being due to ICM emission (right). The dotted circle marks the maximal X-ray/optical separation of 0.439 Abell radii. Data points outside the circle in the right-hand plot represent components of double clusters or clusters with unusually large X-ray to optical separations (see text for details).

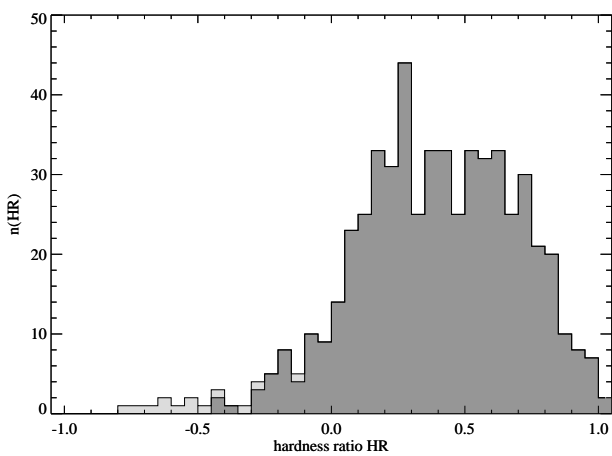


**Figure 11.** The distribution of spectral hardness ratios for the 566 X-ray sources of the decontaminated sample (dark shading). The 13 soft sources highlighted in Fig. 10 are shown in light shading.

the normalization  $\sigma_0$  and the core radius  $r_c$  from the VTP source characteristics. Note that it is only in *correcting* the detected count rates that a specific model for the source profile and, in particular, spherical symmetry is assumed. As this flux correction step is crucial for any flux-limited cluster sample, the procedure applied shall be described in some more detail in the following.

The detected and background corrected count rate  $s$  can be written as

$$s = s(r_{\text{VTP}}) = 2\pi \sigma_0 \int_0^{r_{\text{VTP}}} \tilde{\sigma}(r) r dr. \quad (3)$$

Here,  $r_{\text{VTP}}$  is the effective radius of the emission pattern detected by VTP. The algorithm making no assumptions about the spheric-

ity of sources, the detected emission can essentially be of arbitrary shape.  $r_{\text{VTP}}$  is then given by

$$A_{\text{VTP}} = \pi r_{\text{VTP}}^2,$$

where  $A_{\text{VTP}}$  is the total area covered by the Voronoi cells of all photons assigned to any one source by VTP (see Ebeling & Wiedenmann 1993 for details of the VTP algorithm). The observed surface brightness distribution  $\tilde{\sigma}(r)$  in Eq. 3 is the convolution of the source's intrinsic surface brightness distribution  $\tilde{\sigma}_K$  with the instrument response:

$$\tilde{\sigma}(r) = \int_0^{2\pi} \int_0^\infty \tilde{\sigma}_K(|\vec{r} - \vec{r}'|) \text{PSF}(r') r' dr' d\phi.$$

For the RASS, the telescope's point-spread function,  $\text{PSF}(r)$ , is the weighted average of the PSFs at all off-axis angles.  $\text{PSF}(r)$  has been computed for several photon energies by Hasinger et al. (1994); we employ a numerical representation of  $\text{PSF}(r)$  for  $E = 1 \text{ keV}$  (De Grandi, private communication) that was shown to be in excellent agreement with the source profiles found with RASS-detected AGN (Molendi 1995).

Besides Eq. 3, the second crucial equation is the one specifying how close to the background the surface brightness of the outermost regions of a VTP detection is:

$$\sigma_0 \tilde{\sigma}(r_{\text{VTP}}) = (f - 1) \sigma_{\text{bkg}}. \quad (4)$$

Both the average surface brightness of the background emission,  $\sigma_{\text{bkg}}$ , and  $f$ , the normalised distance of the lowest surface brightness region to the background level, are parameters returned by VTP for each source. From Eqs. 3 and 4, we can thus eliminate  $\sigma_0$  in order to first solve numerically for the core radius  $r_c$ , and then, with  $\tilde{\sigma}'(r_{\text{VTP}})$  known, obtain  $\sigma_0$  from Eq. 4.

Finally, the true total source count rate can be determined from

$$s_{\text{true}} = 2\pi \int_0^\infty \sigma_K(r) r dr = \frac{\pi \sigma_0 r_c^2}{3(\beta - 1/2)}. \quad (5)$$

Note that at no stage of the flux correction procedure the model profile from Eq. 2 is actually fitted to the observed surface brightness distribution. Although we do assume a specific model, it is only its integral properties that enter, which is why deviations of the true distribution from the assumed model have much less effect on the result than they do for the fitting procedures employed by conventional source detection algorithms. The lack of any radial fitting, however, also entails that for any particular cluster the value for the cluster core radius  $r_c$  determined in the flux correction process can not be expected to be as accurate as what might be obtained in a detailed imaging analysis of pointed data. Rather, it should be seen as a statistical parameter that allows the fraction of the cluster emission that has escaped direct detection to be assessed.

Due to the limited spatial resolution of the PSPC, clusters are recognized as extended sources only if their projected effective core radius  $r_c$  exceeds some 15 arcsec. For even more compact sources we compute the flux correction factors from the PSF alone:

$$\frac{s(r_{VTP})}{s_{\text{true}}} = 2\pi \int_0^{r_{VTP}} \text{PSF}(r) r dr. \quad (6)$$

Figure 13 shows the resulting flux correction factors  $s_{\text{true}}/s$  for a King profile convolved with the PSF and the PSF alone (cf. Eqs. 5 and 6) as a function of the core radii  $r_c$  returned by the above procedure. Note how the flux correction factors for extended and point-like sources converge at  $r_c \sim 15''$ .

## 6.2 Correction for flux from point sources and the accuracy of VTP fluxes

The accuracy of the corrected RASS-VTP count rates can be assessed by comparing them to the PSPC broad band count rates obtained in pointed observations (POs) of the same clusters. To this end we retrieve from the ROSAT public archive the PSPC images and exposure maps for 100 clusters with RASS detections at count rates ranging from 0.1 to 10 counts per second in the PSPC broad band. The median exposure time for this set of pointings is 10 ks, the extreme values are 1700 s (comparable to the deepest PET fields from the RASS) for A 76 and 45 ks for A2218.

Total count rates in the PSPC broad band are obtained independently by two of us (HE and ACE) by interactively selecting circular cluster and background regions in the flat-fielded PSPC images. In order to allow the contribution from point sources to the total cluster count rate to be quantified, we determine two count rates per cluster, one from diffuse ICM emission, and a second one from any point sources embedded therein. The background is taken from regions that appear source-free in a vignetting corrected image of the respective PSPC field. For all but the faintest clusters we find the systematic uncertainties of some 5 per cent to dominate over the statistical error of 1 per cent (median) in the obtained count rates. Note that no VTP derived parameters are used in this straight-forward, interactive determination of cluster count rates.

Figure 14 compares the count rates determined from the pointed observations *including point sources* with the corrected RASS-VTP count rates (cf. 6.1). The error bars in Fig. 14 were obtained by adding Poissonian and systematic errors in quadrature; the latter are assumed to be five per cent for VTP and PO count rates alike.

Note that, although the overall distribution is in reasonable agreement with the one-to-one relation expected for perfect agreement between the two data sets (shown as a dotted line in Fig. 14), the count rates obtained from the RASS lie systematically above

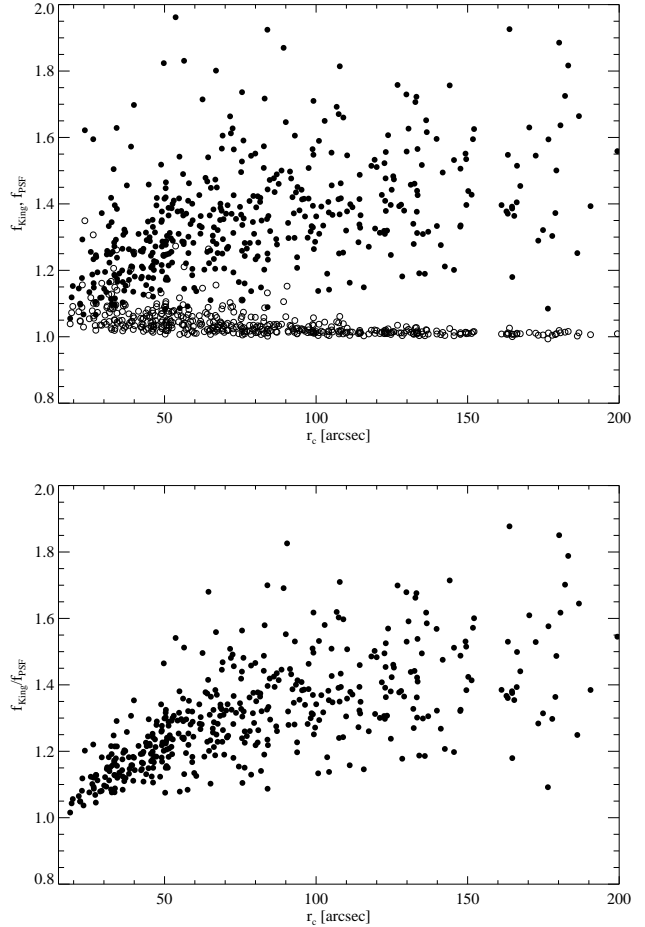


**Figure 13.** The count rate correction factors for our sources as a function of the core radius determined for a King profile. The top panel shows the values obtained when either a convolution between a King law and the instrument PSF (filled circles) or the instrument PSF alone (open circles) is used for a radial surface brightness profile. The bottom plot shows the ratio of the two correction factors and illustrates how both solutions converge for point-like sources, i.e., for core radii below some 20 arcseconds. Eleven sources consisting of less than twenty photons have been omitted from these plots.

the PO values by about nine per cent at all flux levels. This effect is, however, anticipated. At the sensitivity of the RASS, X-ray point sources within a cluster, such as individual galaxies or QSOs, are in general not resolved but blended into the diffuse X-ray emission from the ICM. As a consequence,  $s(r_{VTP})$  in Eq. 3 is an overestimate of the count rate from ICM emission within  $r_{VTP}$ . The overestimation becomes worse when the correction for not directly detection flux, which assumes a pure King profile, is applied to this sum of diffuse and point-like emission. Starting from a contaminated source, the procedure described in Section 6.1 thus over-corrects the missing ICM flux.

The four clusters shown as solid diamonds in Fig. 14 are the ones flagged earlier as possibly considerably contaminated by non-ICM emission *on the basis of their appearance in the RASS alone* (cf. Section 5). They do, however, not stand out particularly in Fig. 14 – in fact, many clusters that lie even higher above the dotted line (indicating the nominal count rate) have not been recognized as contaminated in the RASS data. We therefore resort to correcting

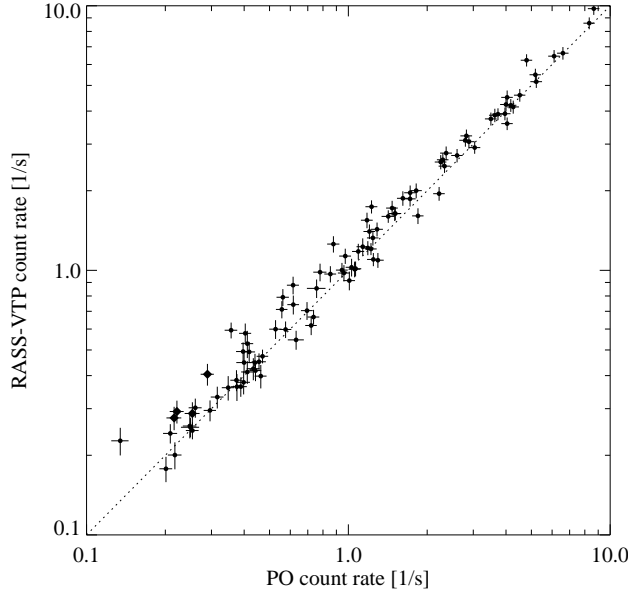


**Figure 14.** PSPC broad band count rates for 100 ACO galaxy clusters as derived from ROSAT All-Sky Survey data using VTP, compared to the corresponding values obtained from pointed observations (PO). Note that the contribution from point sources is *included* in the PO count rates. The error bars allow for a five per cent systematic uncertainty in addition to the Poissonian errors. The four clusters shown as filled diamonds have been marked as probably severely contaminated on the grounds of their appearance in the RASS X-ray images.

for contamination on a statistical rather than on a cluster-by-cluster basis.

As the point-source contamination affects not only the directly detected emission but also, and in a complicated way, the flux correction factor, the resulting systematic overestimation in the total VTP count rates cannot be corrected for straightforwardly. However, there is a simple heuristic solution. With the initially detected VTP count rates being too low and the corrected ones being too high, we adopt their geometrical mean as the best RASS determination of the ICM emission from clusters of galaxies.

These are the final count rates our X-ray flux limited sample is based upon. Figure 15 shows the correlation between the RASS count rates thus corrected and the corresponding PO values where, this time, the point source contribution has been removed. The overall  $1\sigma$  scatter of the data points around the one-to-one relation indicated by the dotted line in Fig. 15 amounts to 15.4 per cent; the mean offset is essentially zero (0.1 per cent). Note that at no flux level there is a systematic trend for the final VTP fluxes to over- or underestimate the true fluxes as represented by the PO values. This can be seen more clearly from Fig. 16 which shows the ratio of VTP to PO count rate as a function of the equivalent VTP source counts; the data are perfectly consistent with a constant value of unity. Figure 16 also shows how the standard deviation in the count rate ratio, which represents the fractional  $1\sigma$  error in our final RASS-VTP count rates, decreases with increasing source photon statistics. From this we find

$$\frac{\Delta s}{s} = 2.29 (s t_{\text{exp}})^{-0.48}, \quad (7)$$

the dashed line in Fig. 16. The overall, relative error of our final

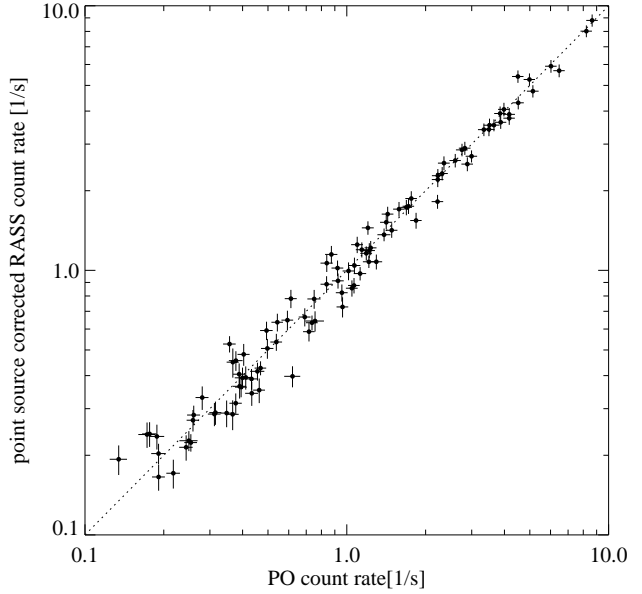


**Figure 15.** PSPC broad band count rates for 100 ACO galaxy clusters as derived from ROSAT All-Sky Survey data using VTP, compared to the corresponding values obtained from pointed observations (PO). Note that the contribution from point sources is *excluded* in the PO count rates. The error bars allow for a five per cent systematic uncertainty in addition to the Poissonian errors.

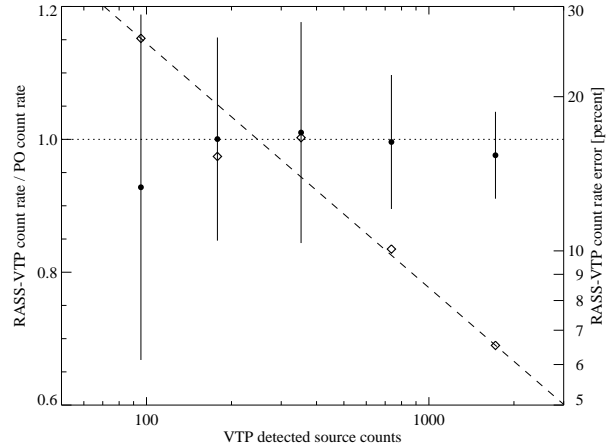


**Figure 16.** Average ratio of the count rates derived from ROSAT All-Sky Survey data using VTP to the corresponding values obtained from pointed observations (filled circles with error bars) as a function of the source counts detected by VTP. The sample is the same as in Figs. 14 and 15. Note the excellent agreement between the two sets of cluster count rates at all source count levels. The open diamonds represent the  $1\sigma$  scatter about this one-to-one correlation – the values refer to the right-hand y axis. The dashed line shows the best power-law fit to the  $1\sigma$  errors.

count rates is thus about twice as high as that expected from photon statistics alone.

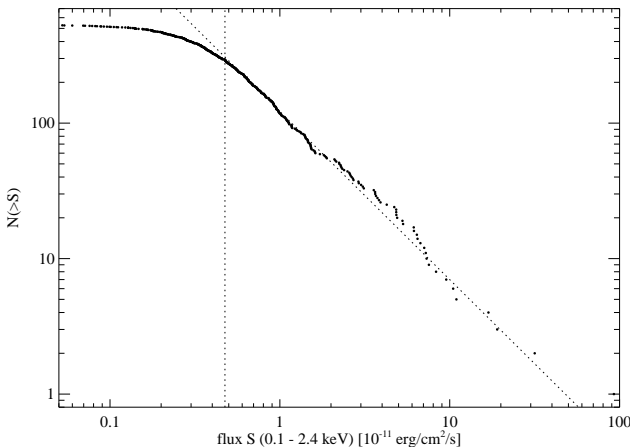


**Figure 17.** The cumulative number count distribution of the 532 X-ray sources constituting our tentative sample as a function of energy flux in the ROSAT 0.1 to 2.4 keV band. The dotted lines show the best-fitting power law of slope  $-1.25$  and the flux limit of  $5.0 \times 10^{-12}$  erg/cm $^2$ /s of a 95 per cent complete sample.

### 6.3 Converting PSPC count rates into fluxes

We convert the corrected count rates to proper energy fluxes using the XSPEC spectral analysis package and assuming a Raymond-Smith type spectrum with a global metal abundance of 30 per cent of the solar value. Values for the Galactic column density of neutral Hydrogen,  $n_{\text{H}}$ , are taken from the compilation of Stark et al. (1992) for declinations north of  $-40$  degrees and from Dickey & Lockman (1990) for the rest of the sky. Where available, measured X-ray temperatures taken from the compilation of David et al. (1993) are used in the conversion (73 clusters); for the remainder the ICM gas temperature is estimated from the clusters' bolometric X-ray luminosity. We adopt

$$kT = 2.55 \text{ keV } L_{\text{X,bol,44}}^{0.354}$$

for the  $kT - L_{\text{X}}$  relation (D.A. White 1996) where  $L_{\text{X,bol,44}}$  is the bolometric X-ray luminosity in units of  $10^{44}$  erg s $^{-1}$ . Starting from a default value of 5 keV,  $kT$  is then determined from the above relation in an iteration loop.

## 7 ESTABLISHING THE XBACS' FLUX LIMIT OF COMPLETENESS

Figure 17 shows a simplified  $\log N - \log S$  diagram, namely the cumulative number of clusters as a function of their 0.1 to 2.4 keV flux. The slope of  $-1.25 \pm 0.04$  of the best fitting power law is somewhat steeper than, but not in conflict with, the  $-1.02 \pm 0.23$  found by Gioia et al. (1984) for the EMSS cluster sample. The quoted slope is determined in a maximum-likelihood fit of a power law to the differential, unbinned representation of the data in the range  $S > S_{\text{min}}$  where  $S_{\text{min}}$  is varied from  $0.7$  to  $1.2 \times 10^{-11}$  erg/cm $^2$ /s. The values of  $-1.25 \pm 0.04$  are the mean and the  $1\sigma$  standard deviation of the power law slopes obtained in this range.

Calling the diagram shown in Fig. 17 a ‘ $\log N - \log S$  distribution’ is actually not quite correct, as it is not properly normalized to the sky area covered at any flux value. This is why we have referred to Fig. 17 as a ‘simplified’  $\log N - \log S$  relation. In order to correctly normalize the distribution, one would have to know

the fraction of sky covered during the RASS at any limiting flux. The quantity that is relevant in this context is in fact not the energy flux, but rather the raw count rate at which a source is initially detected. As was shown in Section 3, sources consisting of at least 13 photons are reliably detected by the SASS. However, in order to determine accurate fluxes for extended sources, we re-analysed the RASS data with VTP (cf. Section 4), and, in the end, included VTP detections of sources that had not been detected by the SASS beforehand. These detections are either of clusters at redshifts below 0.05, where VTP was run on the RASS images of *all* ACO clusters regardless of whether the SASS had detected them or not, or of clusters that lie serendipitously in the  $2 \times 2$  deg $^2$  RASS fields that VTP ran upon.

It is the combination of two different source detection algorithms and also that they analysed data sets of, occasionally, very different exposure times, that make a consistent correction of the  $\log N - \log S$  distribution for sky coverage very difficult. On top of that comes the incompleteness introduced by the selection effects in the underlying optical sample; at the lowest X-ray fluxes, this optical incompleteness is essentially unquantifiable.

Since, however, none of these effects affect the shape of the  $\log N - \log S$  relation at the fluxes used in fitting the power law, we do not attempt at all to correct for variations in the RASS sky coverage and the like, and use our simplified  $\log N - \log S$  distribution only to establish the X-ray flux limit of completeness for our sample.

The completeness limit (95 per cent) derived from Fig. 17 is  $5.0 \times 10^{-12}$  erg/cm $^2$ /s; 277 X-ray sources lie above this threshold constituting our X-ray flux limited sample of Abell and ACO clusters of galaxies. Since this flux limit lies significantly below the flux range over which the power law has been fitted, the latter is not affected by the increasing incompleteness at fainter fluxes.

Figure 18 shows the distribution of total VTP count rates for these 277 sources. Note that the flux limit of  $5.0 \times 10^{-12}$  erg/cm $^2$ /s has no direct equivalent in terms of VTP count rate although it corresponds roughly to 0.27 counts per second (shown as a dotted line in Fig. 18). It is thus crucial that the flux limit is established properly, i.e., with respect to energy fluxes rather than detector count rates. The impact of our initial cut at a SASS count rate of  $0.1 \text{ s}^{-1}$  on the completeness of our sample is discussed in Section 10.1.

The nine clusters classified as double and detected as separate X-ray sources receive a special treatment. Since we can expect more clusters in our sample to be physically double systems, which, however, are not detected as such due to the limited angular resolution of the RASS, we take this selection effect into account by including into the XBACS sample those of our double clusters that would meet the flux criterion if both components were merged, i.e. if they were not resolved as multiple systems by the PSPC. For A 2572 (Ebeling et al. 1995) and A 3528 (Raychaudhury et al. 1991) this turns out to be unnecessary as both components are bright enough to be included as clusters in their own right. For A 548, A 901, A 1631, and A 1750 only the flux of the brighter subcluster exceeds  $5.0 \times 10^{-12}$  erg/cm $^2$ /s; here we include the second component. In the case of A 1758 both components fall below the flux limit but are bright enough to be included when taken together. A 625 and A 2197, finally, are too faint to be accepted even when the flux from both components is summed.

Having thus included one more cluster, the XBACS sample now comprises 276 clusters seven of which are double. Of the total of 283 clusters (or subclusters), 277 fall above the flux limit.

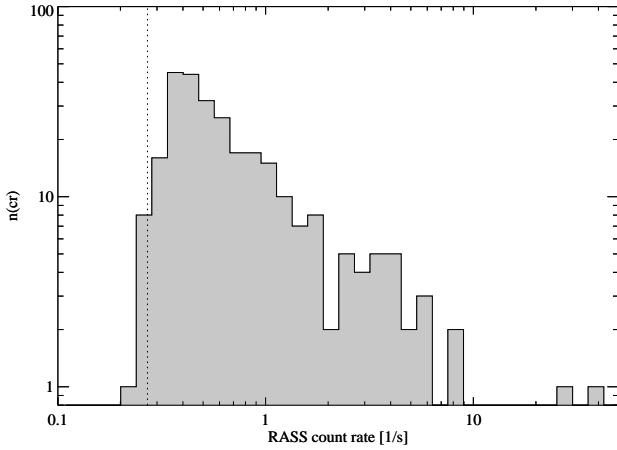


**Figure 18.** The distribution of total VTP count rates for the flux limited sample of XBACs sources. The dotted line at a count rate of  $0.27 \text{ s}^{-1}$  marks the approximate count rate equivalent of the flux limit at  $5.0 \times 10^{-12} \text{ erg/cm}^2/\text{s}$ .

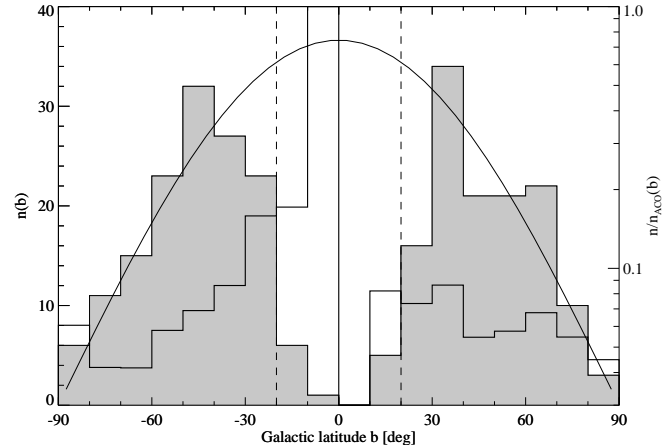
## 8 THE XBACs' GALACTIC LATITUDE DISTRIBUTION

Figure 19 shows the distribution of the XBACs with Galactic latitude  $b$  (shaded) and also the fraction of all ACO clusters the XBACs counts in each Galactic latitude bin correspond to (represented by the bold solid line). The binning ( $\Delta b = 10^\circ$ ) was made rather crude deliberately, in order to wash out all physical large scale structure (the spatial distribution of our clusters is discussed in Paper III of this series). Note that at  $|b| \gtrsim 30^\circ$  the absolute number of clusters in our sample as a function of  $b$  is in good agreement with what is expected for a uniform distribution of clusters on the sky (shown as the fine solid line in Fig. 19). For  $|b| \lesssim 30^\circ$ , however, the numbers fall significantly short of the predicted values for constant cluster surface density. Since galaxy clusters do not cluster on scales of tens of degrees, this effect can not be attributed to intrinsic variations in the cluster surface density, but rather reflects ACO's difficulties in reliable detecting galaxy clusters in the presence of increased Galactic obscuration and stellar density.

As far as the *fraction* of all ACO clusters included in our sample is concerned, we find only a very moderate increase towards the Galactic plane in the northern Galactic hemisphere. However, the picture changes dramatically in the southern Galactic hemisphere, where a steep increase in the fraction of ACO clusters included in our X-ray flux limited sample is observed within a separation of  $\sim 30^\circ$  of the Galactic plane. This suggests that, in the south, ACO's selection was biased in the sense that, with decreasing Galactic latitude, they included preferentially rich and compact (i.e., potentially X-ray luminous) systems in their catalogue.

In order to remain consistent with previous studies (e.g. Piccinotti et al. 1982, Edge et al. 1990, Gioia et al 1990, Henry et al. 1992), we restrict ourselves to sky areas at high Galactic latitude, i.e.  $|b| \geq 20^\circ$  (see the dashed lines in Fig. 19). Although in regions that far away from the Galactic plane the incompleteness of the ACO cluster sample due to Galactic obscuration is small, it is nonetheless still noticeable (cf. Fig. 19). In order to assess the impact of the incompleteness remaining in the range  $20^\circ \leq |b| \leq 30^\circ$  we flag these clusters in our final list (see Table 3) and test empirically whether the results presented in the following papers of this series are affected by our including them or not.

The sky coverage of the high galactic latitude subsample at



**Figure 19.** The differential Galactic latitude distribution of the 276 clusters of our sample of X-ray bright Abell-type clusters (shaded). The bold solid line shows to which fraction of all ACO clusters the value for each Galactic latitude interval corresponds; the fine solid line indicates the run expected for a uniform distribution of clusters on the sky.

$|b| \geq 20^\circ$  can be approximated by the geometrical solid angle, i.e.  $4\pi$  minus the solid angle covered by a 40 degree wide band representing the Galactic plane. Subtracting another  $50 \text{ deg}^2$  to take into account the extragalactic sky obscured by the Magellanic Clouds yields a solid angle of  $8.25 \text{ sr}$ .

14 clusters out of the 532 featured in the simplified  $\log N - \log S$  distribution shown in Fig. 17 are at  $|b| < 20^\circ$ ; the fluxes of 12 of them exceed the flux limit of completeness at  $5.0 \times 10^{-12} \text{ erg/cm}^2/\text{s}$ . If all 14 are excluded from the sample before the power law is fitted to the  $\log N - \log S$  distribution, the best fitting slope comes out slightly steeper at  $-1.28 \pm 0.04$  which is mainly due to the well-known fact that 3 of the 6 X-ray brightest ACO clusters (A 426, A 3627, and A 2319) are at low Galactic latitude. When the low Galactic latitude clusters are excluded, the flux limit of completeness increases somewhat from  $5.0$  to  $5.3 \times 10^{-12} \text{ erg/cm}^2/\text{s}$  which would exclude 16 clusters more. It thus makes a difference for the XBACs sample whether the flux limit or the galactic latitude cut is applied first. We adopt the former procedure and are left with 271 X-ray sources corresponding to 264 Abell-type clusters.

If finally only clusters at  $|b| \geq 30^\circ$  are considered, the power law of the  $\log N - \log S$  distribution of Fig. 17 continues to steepen; the best-fitting slope is  $-1.46 \pm 0.03$ . Much of this steepening is, however, again mainly due to a few very X-ray bright (i.e. local) clusters lacking from the high Galactic latitude sample. No more than about three additional clusters at fluxes  $\gtrsim 10^{-10} \text{ erg cm}^2 \text{ s}^{-1}$  are required to make the best fitting slope power law consistent with the value of  $-1.24$  found for the  $\log N - \log S$  distribution of the overall sample. The apparent steepening of the  $\log N - \log S$  power law can thus be explained entirely by, e.g., a statistically insignificant dearth of optically rich enough clusters within a redshift of  $\sim 0.02$ .

## 9 THE XBACs' REDSHIFT DISTRIBUTION

As mentioned earlier, the ACO catalogue is known to suffer from various selection biases inherent to the procedures employed to find clusters in the optical. In particular, the probability of a cluster being included in the ACO catalogue is a strong function of redshift:

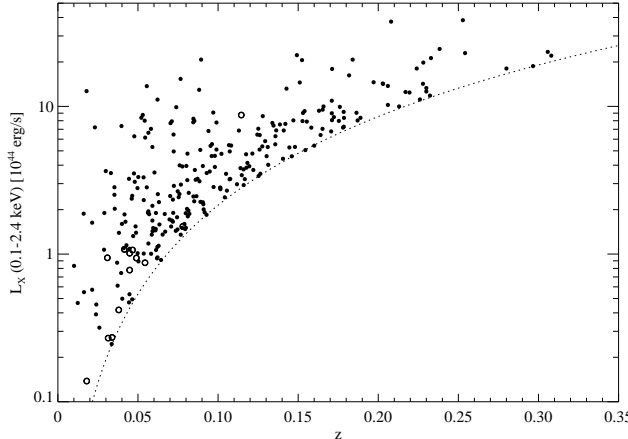


**Figure 20.** The X-ray luminosities of the 276 clusters of our flux limited sample of X-ray bright Abell-type clusters (no Galactic latitude cut) as a function of redshift. The dotted line illustrates the cutoff introduced by the X-ray flux limit at  $5.0 \times 10^{-12}$  erg/cm $^2$ /s. The thirteen VTP detected clusters with original SASS count rates of less than  $0.1 \text{ s}^{-1}$  are plotted as open circles.

The more distant an Abell cluster, the richer and more compact it has to be to be recognized as such on the optical plates. Although the ACO catalogue was designed to be volume complete out to a limiting redshift of  $z = 0.2$ , this goal has been achieved only for the richer systems. Clusters in richness class 0 and 1 start to become undersampled at redshifts of about 0.13 (e.g. Huchra et al. 1990, Scaramella et al. 1991, Ebeling et al. 1993), i.e. at redshifts higher than that the ACO catalogue is volume complete only for the richest systems. In an X-ray flux limited sample, however, the correlation between optical richness and X-ray luminosity (Briel & Henry 1993; see also Paper II of this series) tends to counteract this selection effect.

Figure 20 illustrates this by showing the XBACs' X-ray luminosity as a function of redshift: At low and intermediate redshifts where the ACO catalogue is indeed volume complete, all luminosity and richness classes get included. With increasing redshift, however, the X-ray flux limit selects increasingly luminous (and intrinsically rich) systems disregarding the poorer systems. It is only for the latter, however, that the ACO catalogue becomes seriously incomplete at redshifts around 0.13. Consequently, we can expect our sample to remain unaffected by the incompleteness of the ACO catalogue out to redshifts considerably beyond the quoted value of 0.13.

Plotting the redshift histogram for our flux limited sample (Fig. 21) we find the absolute number of clusters per redshift bin to drop smoothly with  $z$ . The fraction of ACO clusters included in our sample in each redshift bin, however, starts to rise at about  $z = 0.2$ , indicative of a severe volume incompleteness of the underlying optical catalogue *if all richness classes (including 0) are considered*. This rise in the fraction of X-ray detected clusters occurs at much lower redshifts if no flux limit is imposed (Ebeling et al. 1993).

In order to minimize any remaining impact of the overall incompleteness of the underlying optical catalogue onto our X-ray flux limited sample we restrict its redshift range to the nominal completeness limit of the ACO catalogue at  $z = 0.2$ . The resulting, ‘statistical’ XBACs sample consists of 242 clusters at  $|b| \geq 20^\circ$ , six of which are marked as double (the seventh double cluster, A 1758,

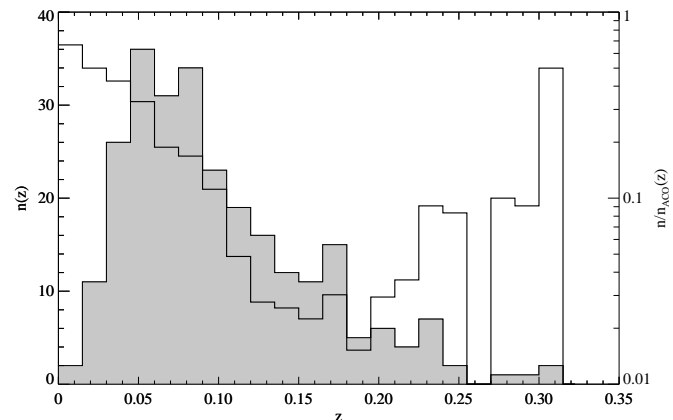


**Figure 21.** The differential redshift distribution of the 264 clusters of our sample of X-ray bright Abell-type clusters at  $|b| \geq 20^\circ$  (shaded). The bold line shows to which fraction of all ACO clusters the value for each redshift interval corresponds. Both measured and estimated redshifts have been used.

at a redshift of 0.28 is now excluded). The issue of possible incompleteness introduced into the XBACs sample by the volume incompleteness of the ACO catalogue is discussed in more detail in Section 10.

## 10 THE COMPLETENESS OF OUR SAMPLE

Several effects limit the completeness of our flux limited sample most of which are intrinsic to the way the XBACs have been selected in the X-ray. Besides that, there is, however, also the important question as to which extent the XBACs sample is affected by the volume incompleteness of the optical ACO cluster catalogue.

### 10.1 Incompleteness introduced in the X-ray selection procedure

As far as the compilation of our sample in the X-ray is concerned, there are four sources of incompleteness.

First of all, there is the dependence of the RASS sky coverage on the exposure time mentioned in Section 4. At the chosen minimal exposure time of 130 s, the sky coverage is 95 per cent.

Secondly, clusters are missing from our sample due to the systematic positional differences between the centroids of the clusters’ galaxy distribution which determine the optical cluster positions and the centres of the clusters’ gravitational potential wells which is what the X-ray positions correspond to. These differences are reflected in the fact that a small fraction of true coincidences between ACO cluster positions and RASS X-ray sources are found at respective separations greater than  $0.439 r_A$  (see Fig. 9). The completeness of our sample with respect to this effect is limited by the finite cut-off in the allowed X-ray/optical separation and amounts, again, to 95 per cent.

Thirdly, clusters may be missing from our sample due to the imperfections of the SASS source detection algorithms mentioned earlier. At redshifts smaller than 0.05 this is not an issue since the PET data around *all* ACO clusters in that redshift range have been reprocessed by VTP. At higher redshifts, however, clusters that should be in our flux limited sample may be missing because

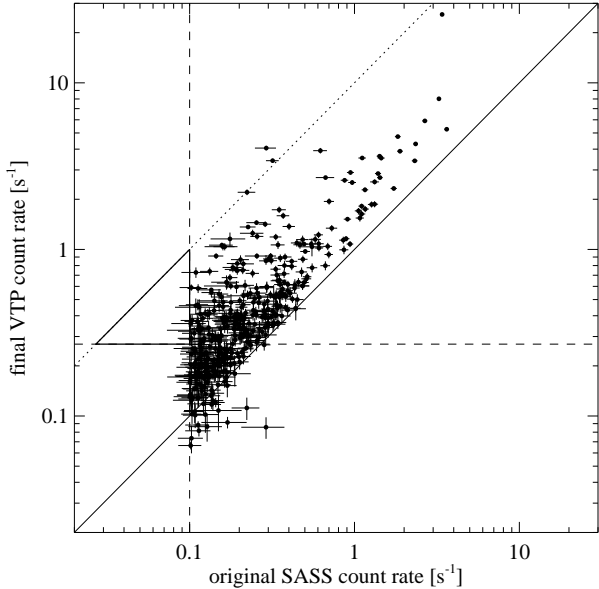


**Figure 22.** The relation between original SASS and final VTP count rates for 425 ACO clusters detected by both algorithms; the error bars represent photon statistics only. The dashed lines mark the initial SASS count rate threshold at  $0.1 \text{ s}^{-1}$  and the approximate VTP count rate equivalent of the XBACs flux limit at  $0.27 \text{ s}^{-1}$ . The bold triangle indicates the region where clusters missing from the XBACs sample are expected to lie.

the SASS returned count rates that were too low by more than a factor of  $\sim 3$ . This can be said because the flux limit of our sample of  $5.0 \times 10^{-12} \text{ erg/cm}^2/\text{s}$  corresponds approximately to a VTP count rate of  $0.27 \text{ s}^{-1}$  (cf. Fig. 18), i.e., a value about three times higher than the threshold of  $0.1 \text{ s}^{-1}$  applied to the initial RASS source list delivered by the SASS. The incompleteness introduced by this effect can be estimated from the distribution of SASS and VTP count rates for clusters detected by both algorithms.

Figure 22 shows this distribution; the respective count rate limits are shown as dashed lines. The triangle on the left of the plot delineates the section of parameter space where clusters missing from our sample reside. Extrapolating from the density of data points to the upper right of this area, we estimate the number of clusters in this region to be less than 31. Since 13 of those have entered our sample as VTP detections either at low  $z$  (ten clusters) or serendipitously at redshifts above 0.05 (three), the total number of potentially missing cluster comes down to less than 18, i.e., the completeness of our sample with respect to this effect is at least 93 per cent.

That this value is indeed a lower limit can be seen from an alternative approach. For any cluster featuring a SASS count rate of less than  $0.1 \text{ s}^{-1}$ , the final VTP count rate would have to be higher by at least a factor of 2.7 for it to be included in the XBACs sample. How likely is this to happen? Figure 23 shows this count rate ratio as a function of redshift for the clusters that have both SASS and VTP count rates (top panel) and for those that make it into the XBACs sample before the redshift cutoff at  $z = 0.2$  is applied (bottom panel). Of the 425 ACO cluster whose count rates are shown in Figs. 22 and 23 (top panel) no more than 76 fulfill this criterion; 26 of them (i.e. about one third) have redshifts less than 0.05. Since we know that at redshifts below 0.05 the XBACs sample is complete by design, and that the number of clusters with  $z \leq 0.05$  that made

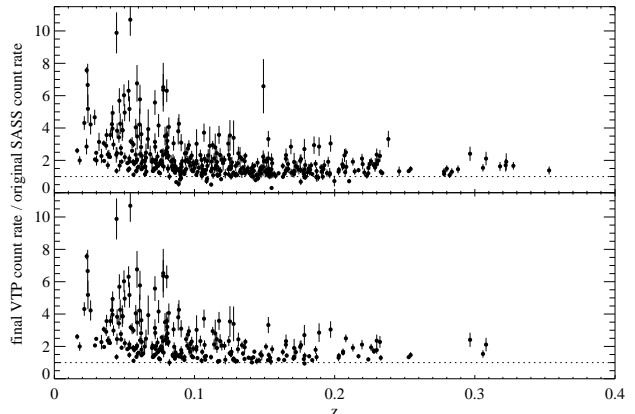


**Figure 23.** The ratio of final VTP count rate to original SASS count rate as a function of  $z$  for the 425 ACO clusters detected by both algorithms (top panel). The lower panel shows the same distribution for the clusters that got included in the final XBACs list before the redshift cutoff is introduced. In both panels the error bars represent photon statistics only.

it into the sample coming from an initial SASS count rate of less than  $0.1 \text{ s}^{-1}$  is ten, we can extrapolate to a total number of 29 clusters that should get included despite their SASS count rates falling short of the threshold value. 13 of these 29 have been detected by VTP, so that no more than about 16 can be missing. Consequently, we arrive at an incompleteness of at most six per cent due to our initial cut in the SASS count rate, consistent with the above estimate. From the positions of the 13 additional VTP detections in the  $L_X - z$  distributions of Fig. 20 we conclude that the vast majority of the missing clusters should feature low X-ray luminosities, and in any case lie close to the XBACs' flux limit.

According to the distribution shown in Fig. 23, 11 of the 16 clusters that could be missing can be expected to lie in the redshift range from 0.05 to 0.1; the remaining five are anticipated to be at  $0.1 < z \leq 0.2$ . The only safe way to find all missing clusters would be to follow the approach taken for the nearby systems at  $z \leq 0.05$ , i.e., re-process the PET fields around *all* ACO fields with VTP. This, however, is clearly prohibitive in view of the massive overhead involved: just within  $z = 0.1$ , 446 *additional* PET fields would have to be re-processed and checked for non-cluster sources to detect the ten clusters possibly missing in that redshift range.

Fourthly and finally, our sample is incomplete due to the X-ray flux limit which was set at 'only' 95 per cent completeness.

Since all these effects are most probably statistically independent, we can simply multiply the corresponding percentages to find the overall completeness of our sample of X-ray bright Abell-type clusters of galaxies (XBACs) to be about 80 per cent. For the reasons detailed above, we believe that this figure comes very close to the maximum value achievable for such a sample.

## 10.2 The impact of optical selection effects

As mentioned in Section 9, the X-ray flux limit of the XBACs sample ensures that, with increasing redshift, more and more luminous clusters are selected (Fig. 20). As a consequence, our sample is, to first order, unaffected by the growing volume incompleteness in the lower Abell richness classes. At any redshift, the clusters miss-

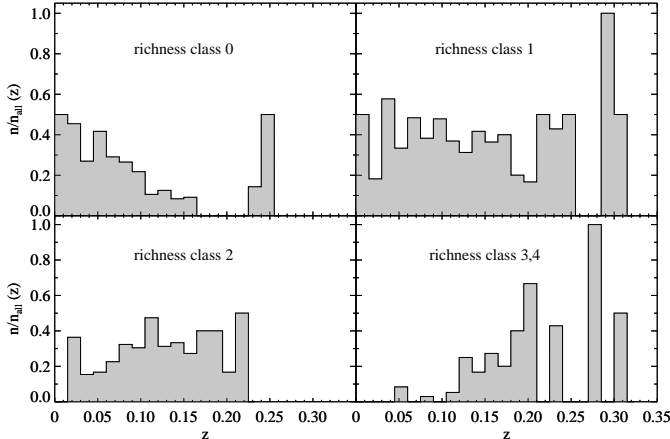


**Figure 24.** The fraction of XBACs (no redshift cut applied) in different Abell richness classes as a function of redshift.

ing from the ACO catalogue would not have been X-ray luminous enough anyway to get included in the XBACs sample.

Figure 24 illustrates once more how the  $L_X - n_{\text{gal}}$  correlation in combination with the X-ray flux limit ensures that the incompleteness in poor clusters at high redshift does not affect our sample. (We drop the redshift limit at  $z = 0.2$  for the purpose of this exercise.) Note how the higher richness classes dominate more and more as redshift increases; the optically poorer clusters which tend to be under-represented in the ACO catalogue at its upper redshift end do not enter the XBACs sample.

It is also noteworthy, however, that of the 13 XBACs at redshifts higher than 0.225, eight have been classified by ACO as richness 0 or 1 systems. Given that the X-ray luminosity of all of them exceeds  $10^{45}$  erg s $^{-1}$ , it is clear that this classification must grossly underestimate these systems' true richness. On the other extreme, we expect the richness of some of the richness class 2 and 3 systems at redshifts below 0.05 to be overestimated. For two ACO clusters in that richness and redshift range this is indeed confirmed by spectroscopic follow-up observations which yield velocity dispersions of the cluster galaxies that are more typical of richness class 1 systems (Ebeling & Mendes de Oliveira, in preparation).

We conclude that at redshifts below about 0.05 our sample is probably even more heavily dominated by optically poor clusters than is apparent from Fig. 24. At redshifts beyond  $\sim 0.15$ , however, where ACO's optical cluster richness starts to be systematically underestimated, the majority of the XBACs are in fact of richness class 2 or greater.

Figure 25 shows again the redshift distribution of the XBACs sample (cf. Fig. 21); this time, however, only the 99 clusters with  $n_{\text{gal}} \geq 80$  (i.e., richness classes 2 and greater) are considered which dominate the sample at  $z \gtrsim 0.15$ . Note that for these rich and X-ray luminous systems the ACO catalogue is actually complete out to redshifts of about 0.23.

It is thus the X-ray flux limit that makes all the difference when we ask what impact the optical selection effects have on an X-ray selected sample: The lower the X-ray flux limit, the more low richness clusters get included and the higher is the risk of becoming affected by the volume incompleteness of the optical catalogues. Consequently, the impact of optical selection effects is strongest for deep X-ray samples with no single, overall flux limit like the ones

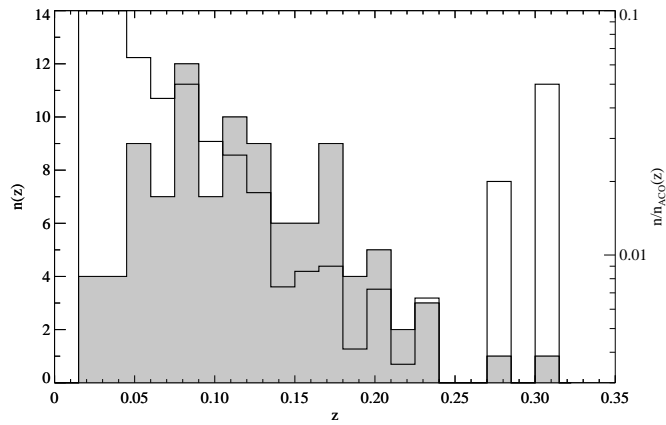


**Figure 25.** The differential redshift distribution (before the redshift cut at 0.2 is applied) of the 99 XBACs at high Galactic latitude and with Abell richness greater than or equal to 2. The bold line shows to which fraction of all ACO clusters in the same richness classes the value for each redshift interval corresponds. Both measured and estimated redshifts have been used.

used in the most recent studies on the X-ray properties of Abell clusters (Briel & Henry 1993, Burg et al. 1994).

As far as the XBACs are concerned, we cannot exclude rigorously that some incompleteness due to the imperfections of the underlying optical catalogue remains. However, based on the above we believe it safe to assume that any remaining incompleteness will be at redshifts below  $\sim 0.1$ . At such low to intermediate redshifts and X-ray luminosities around and below  $10^{44}$  erg s $^{-1}$  we may be missing a few clusters that should be in the ACO catalogue on the ground of their optical richness and are, at the same time, sufficiently X-ray luminous to be included in the XBACs sample. The Virgo cluster, explicitly excluded from Abell's catalogue because of its large angular extent, is one such case (see Böhringer et al. 1995 for a discussion of the RASS data).

## 11 THE XBACs X-RAY SOURCE EXTENT DISTRIBUTION

In principle, the ideal X-ray selection criterion for the compilation of a cluster sample is the X-ray source extent. Even at a redshift of  $z = 0.3$ , a metric cluster core radius of 250 kpc still corresponds to 45 arcsec on an angular scale. Since this is well above the spatial resolution of some 20 arcsec attained typically in the RASS, the X-ray emission from clusters of galaxies is expected to be recognized as extended over the whole redshift range of the XBACs sample. However, in practice the efficiency of a source selection by X-ray extent depends heavily on the sources' brightness and also on the detection algorithm used.

Although the source extent is not utilized for the compilation of the XBACs sample, it is relevant for future, X-ray selected samples such as the ROSAT Brightest Cluster Sample (BCS, Ebeling et al. 1996), the compilation of extended RASS sources discussed by Giacconi & Burg (1993), and the ESO Key Programme on ROSAT clusters in the southern hemisphere (Guzzo et al. 1995).

SASS determines source fluxes by fitting a radial Gaussian profile to the observed spatial photon distribution in a maximum-likelihood procedure. The extent parameter returned for each source is essentially the width of this Gaussian that is in excess

of the width of the instrumental point spread function (Cruddace et al. 1991). At a threshold value of 35 arcsec for the Gaussian source extent, half of all ACO clusters but less than 7 per cent of the non-cluster sources detected by the SASS in the RASS are classified as extended (Ebeling et al. 1993). A lower extent threshold results in an only marginally higher fraction of extended clusters while increasing dramatically the number of point sources that are erroneously classified as extended. If only sources with SASS count rates higher than  $0.1 \text{ s}^{-1}$  are considered (namely the 425 of Fig. 22), the fraction of ACO clusters detected as extended by the SASS rises to some 73 per cent. Within  $z = 0.3$ , this percentage is essentially independent of cluster redshift (dotted curves in Fig. 26). As the SASS count rate correlates only poorly with the true cluster count rate (cf. Fig. 22), the fraction of clusters detected as extended by the SASS does not increase any further when the XBACs flux limit is applied. Lowering the extent threshold does not change much either: even for a threshold value as low as 10 arcsec the overall figure remains essentially the same (77 per cent).

Note that these values are actually upper limits since they do not take into account the 13 XBACs that were missing altogether from the SASS source list that we started from. For the XBACs within  $z = 0.05$  these SASS non-detections introduce an *additional* incompleteness of 20 per cent. The reduced detection efficiency of the SASS at low redshifts is likely to result in an even more severe incompleteness when clusters poorer than those compiled by ACO are considered.

VTP determines a count rate correction factor by comparing the directly detected count rate with that expected from an idealized cluster (see Section 6.1). Besides the actual correction factor, this procedure also returns the angular equivalent of the cluster X-ray core radius. It turns out (Ebeling et al., in preparation) that for this VTP source extent the transition between clusters and point-like X-ray sources occurs at the same numerical value (35 arcsec) as before for the SASS. The fraction of VTP extended sources in the subset of 425 ACO clusters detected by both SASS and VTP is 79 per cent. It depends on the cluster redshift in the sense that nearby systems are more likely to be recognized as extended than distant ones (solid curves in Fig. 26). When the XBACs flux limit is applied, the fraction of clusters classified as extended by VTP rises to some 80 per cent at  $z = 0.3$ ; within a redshift of 0.05 100 per cent are detected as extended. The overall fraction of XBACs clusters in the flux limited sample that are detected as extended by VTP exceeds 90 per cent.

At redshifts higher than, say,  $z = 0.15$ , SASS and VTP are similarly efficient in detecting clusters as extended sources. However, the systems they classify as extended are not the same. The dashed lines in Fig. 26 illustrates the complementarity of the two algorithms by showing the fraction of clusters recognized as extended by either SASS or VTP (or both). Only four out of the 245 clusters that the right-hand plot in Fig. 26 is based upon are not extended if the SASS and VTP extended samples are combined.

To summarize, we find the X-ray source extent to be a useful parameter for the selection of clusters of galaxies from RASS data. For a minimum value of 35 arcsec for the extent parameter and for sources well above the detection limit, the efficiency is some 70 per cent for both SASS and VTP *for clusters at  $z \gtrsim 0.12$* . At lower redshifts, any compilation based on SASS source extent alone will be missing more than one in five ACO clusters (and most probably a much higher fraction of optically poorer systems). For really nearby clusters ( $z \lesssim 0.05$ ) the relative insensitivity of the SASS detection algorithms to low surface brightness emission may result in a deficiency of more than 40 per cent in the number of the de-

**Table 3.** not available for preprinting – sorry!

tectable extended cluster sources. This incompleteness can not be overcome by the introduction of an X-ray flux limit. If the VTP extent parameter is used, the incompleteness of a cluster sample selected by X-ray extent can be reduced to less than 9 per cent at  $z \lesssim 0.12$ ; for the X-ray flux limited XBACs sample, the overall incompleteness within  $z = 0.3$  would be less than 10 per cent if only VTP extended sources were considered.

If, finally, the extent values from both algorithms are combined, essentially all XBACs (98 per cent) are classified as extended.

## 12 XBACS – THE SAMPLE

Table 3 lists our statistical sample of the 242 X-ray brightest Abell-type clusters (XBACs) with Galactic latitudes  $|b| \geq 20^\circ$ , within a redshift of 0.2, and with 0.1 to 2.4 keV fluxes greater than  $5.0 \times 10^{-12} \text{ erg cm}^{-2} \text{ s}^{-1}$ . Six of these 242 systems consist of two separate subclusters. 92 per cent of the clusters in this sample have measured redshifts. We also include the 12 clusters at low Galactic latitude (marked with a  $\bullet$  symbol in the first column) and the 24 clusters at redshifts greater than 0.2 (marked with a  $\star$  symbol) that meet the flux criterion.

In detail the contents of Table 3 are

- column 1: redshift, low Galactic latitude, and contamination flag. Clusters at  $|b| < 20^\circ$  ( $20^\circ < |b| < 30^\circ$ ) are marked  $\bullet$  ( $\circ$ );  $\star$  indicates that the cluster is at  $z > 0.2$  and thus not a member of our statistical sample; ‘c’ means a significant fraction of the quoted flux may come from embedded point sources.
- column 2: ACO name. Where clusters appear to consist of two components, two entries (‘a’ and ‘b’) are listed.
- column 3: Right Ascension (J2000) of the X-ray position as determined by VTP.
- column 4: Declination (J2000) of the X-ray position as determined by VTP.
- column 5: Column density of Galactic Hydrogen from Stark et al. (1992) for  $\delta \geq -40^\circ$  and Dickey & Lockman (1990) for the remainder of the sky.
- column 6: RASS exposure time (accumulated).
- column 7: PSPC count rate in PHA channels 11 to 235 originally detected by VTP.
- column 8: The equivalent radius  $\sqrt{A_{\text{VTP}}/\pi}$  of the source detected by VTP.
- column 9: Final PSPC count rate in PHA channels 11 to 235 based on the original VTP count rate. Statistical corrections for low-surface brightness emission that has not been detected directly and for contamination from point sources have been applied.
- column 10: Error in the final PSPC count rate according to Eq. 7. The fractional uncertainty in the energy flux (column 13) and the X-ray luminosity (column 14) can be assumed to be the same as the fractional count rate error.
- column 11: ICM gas temperature used in the conversion from count rates to energy fluxes. ‘e’ indicates the temperature has been estimated from the  $L_X - kT$  relation.
- column 12: Redshift. ‘e’ indicates the redshift has been estimated from the magnitude of the tenth-ranked cluster galaxy.

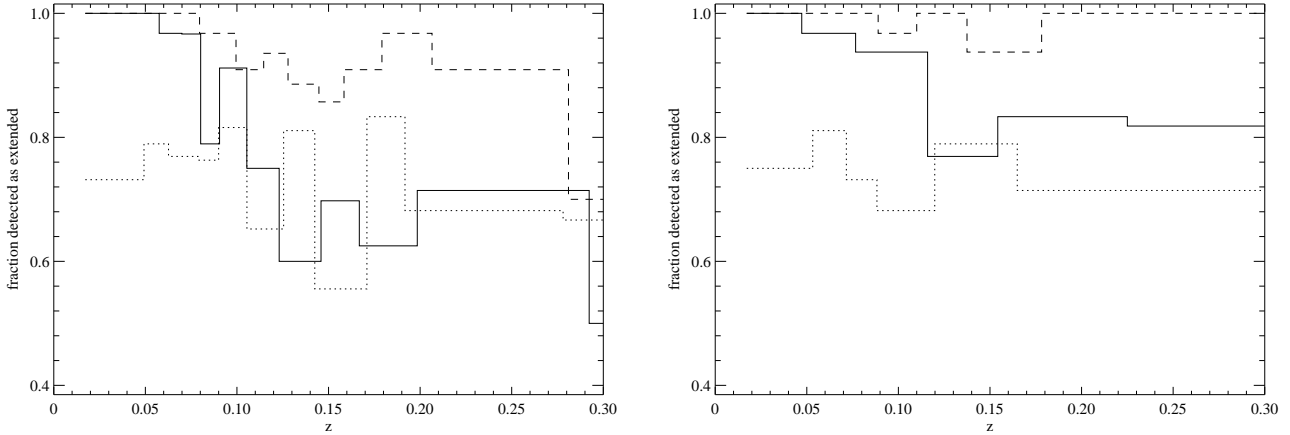


**Figure 26.** The fraction of ACO clusters detected by both SASS and VTP that feature an X-ray source extent of more than 35 arcsec as a function of cluster redshift. In the left hand plot all 425 clusters shown in Fig 22 are included. The right hand graph uses only the 245 ACO clusters that remain when the XBACs flux limit is applied. In both plots, each redshift interval (except the very last one) contains 30 clusters; the VTP curves are shown as solid lines, the SASS data as the dotted lines, and the dashed lines represent the fraction of clusters classified as extended by either or both of the two algorithms.

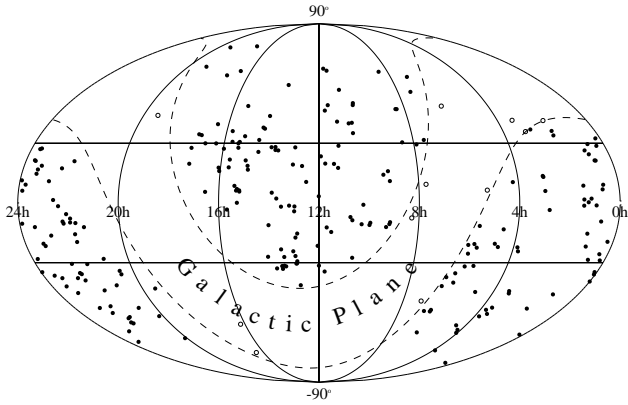


**Figure 27.** The distribution of the 242 clusters in the statistical XBACs sample on the sky (filled circles). The 11 clusters at low Galactic latitude (and  $z \leq 0.2$ ) that have been excluded from the sample are shown as open circles.

- column 13: Unabsorbed X-ray energy flux in the 0.1 to 2.4 keV band.
- column 14: Intrinsic X-ray luminosity in the 0.1 to 2.4 keV band (rest frame).
- column 15: Reference for the redshift in column 8.

To facilitate the comparison with previous flux limited samples, we list in Table 4 the 2 – 10 keV fluxes of the XBACs. The conversion from the PSPC detection band was performed using a Raymond-Smith type spectrum with constant metallicity of 30 per cent of the solar value and values for the neutral Hydrogen column densities and ICM gas temperatures as given in Table 3.

Figure 27 shows the distribution of the XBACs on the sky in equatorial coordinates.

### 13 SUMMARY

In this first paper of a series investigating the properties of the X-ray brightest Abell-type clusters detected in the ROSAT All-Sky Survey (RASS) we present the sample and describe its compilation.

The flow diagram in Fig. 28 gives an overview of the compilation procedure, from the master list of RASS X-ray sources detected by the SASS to the final XBACs sample selected from VTP detections.

The VTP re-analysis of the RASS photon data is a crucial step in the compilation of the XBACs sample. VTP is a source detection and characterization algorithm developed by one of us (HE) to detect overdensities of essentially arbitrary shape in the exposure normalized surface density of RASS photons. Since VTP makes no assumptions about the source geometry (such as sphericity or radial flux profile) it is particularly well suited for the detection and characterization of extended and potentially irregular emission from clusters of galaxies.

The VTP analysis includes a correction of the initial count rates for low-surface brightness emission that has escaped direct detection. This correction takes into account the PSPC point spread function in the RASS and assumes a King law for the generalized radial surface brightness profile. The contribution from point sources embedded in the diffuse cluster emission is corrected for by adopting the geometrical mean of the raw and the corrected count rate values as the final count rate from diffuse ICM emission. A comparison of these final VTP values with the best count rate determinations from archival, pointed PSPC observations for 100 selected clusters shows no systematic differences for count rates ranging from 0.1 to  $10 \text{ s}^{-1}$ ; the total  $1\sigma$  uncertainty in the VTP count rates is about twice as high as that from photon statistics alone.

When comparing the VTP cluster count rates with the respective SASS values we find the SASS count rates to underestimate the true cluster brightness by typically a factor of 0.60 (median) with the 25<sup>th</sup> and 75<sup>th</sup> percentiles being 0.43 and 0.75.

Although the source extent is not used in the compilation of the XBACs sample, we investigate its significance for future compilations of purely X-ray selected samples. A comparison of the extent parameters returned by the SASS and VTP shows that, at redshifts greater than 0.12, both algorithms successfully detect some

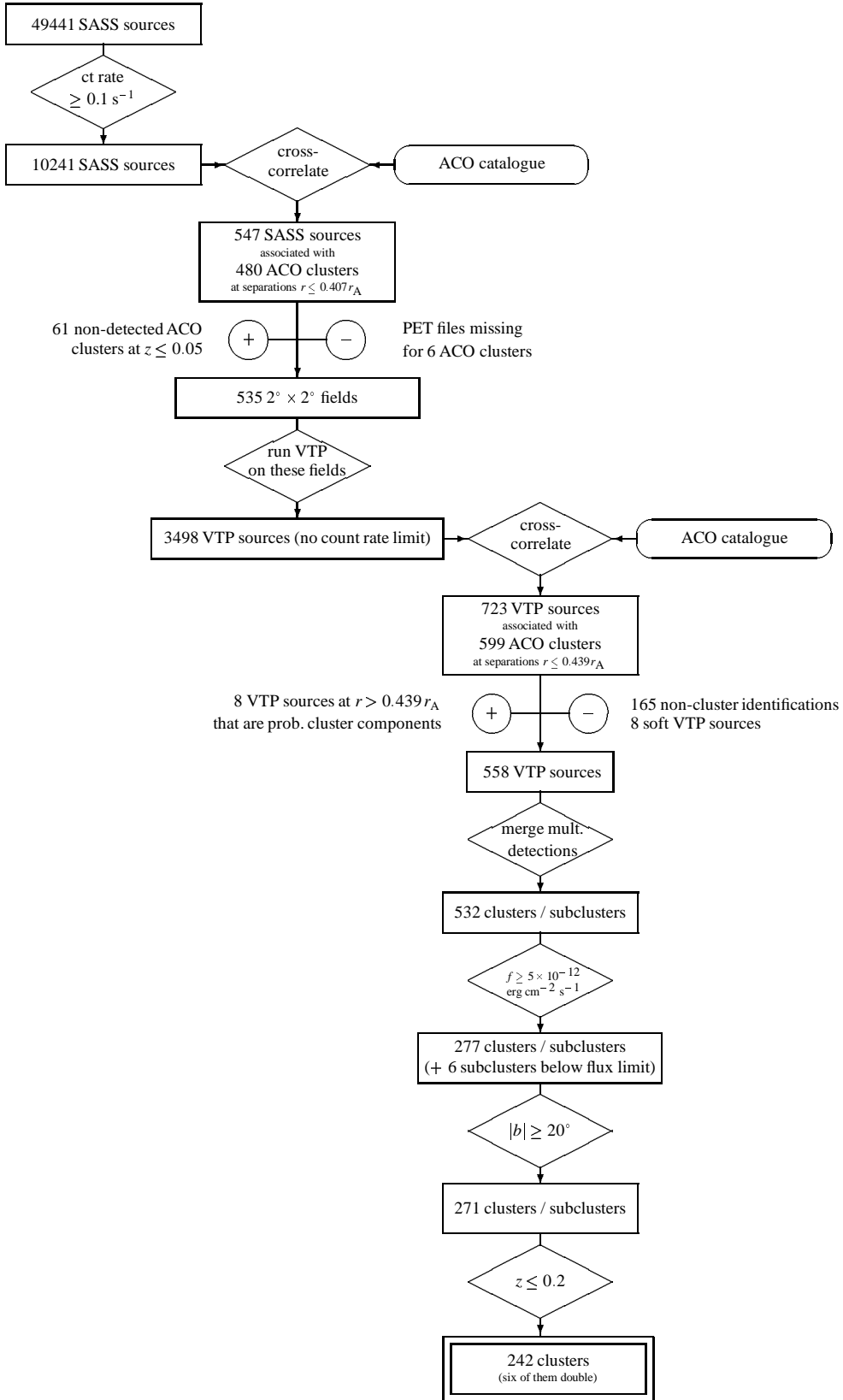


Figure 28. Flow diagram summarizing the compilation of the XBACs sample

**Table 4.** not available for preprinting – sorry!

70 per cent of our ACO clusters as extended X-ray sources. At lower redshifts, VTP has a higher efficiency (approaching 100 per cent at  $z \sim 0.05$ ). If the extent information from both algorithms are combined, essentially all XBACs are classified as extended by at least one method irrespective of redshift.

The sample compiled from VTP detections after non-cluster sources have been discarded consists of 277 clusters (or subclusters) above a flux limit of completeness (95 per cent) of  $5.0 \times 10^{-12}$  erg cm $^{-2}$  s $^{-1}$ . Six more sources with X-ray fluxes below this value are included as subclusters of systems whose brightness exceeds the flux limit when both components are combined.

In order to remain consistent with previous studies, we limit our statistical sample to clusters at  $|b| \geq 20^\circ$  and within the nominal volume of completeness of the ACO catalogue, i.e. to redshifts lower than 0.2. This leads to our final sample of the 242 X-ray brightest Abell-type clusters (XBACs) from the ROSAT All-Sky Survey, 92 per cent of which have measured redshifts. The sample's overall completeness is 80 per cent; in view of the complicated selection procedure, we believe this figure to come close to the maximum value achievable for such a sample. As, at its high redshift end, our X-ray flux limited sample is intrinsically dominated by very X-ray luminous and optically rich clusters, the volume incompleteness in poor clusters of the underlying optical catalogue does not affect the XBACs.

The XBACs constitute the largest X-ray flux limited sample of clusters of galaxies compiled to date. By design, the sample is not only essentially complete but also free from contamination by non-cluster X-ray sources. In the following papers of this series the XBACs' properties are investigated in detail.

## ACKNOWLEDGEMENTS

The authors would like to thank the ROSAT team at MPE for obtaining, processing, and providing the RASS X-ray data this analysis is based upon, and especially Cristina Rosso for her tireless efforts in the RASS PET file retrieval. The ROSAT project is funded by the Bundesministerium für Forschung und Technologie (BMFT) and supported by the Max-Planck-Gesellschaft zur Förderung der Wissenschaften (MPG).

Discussions with Heinz Andernach, Sabrina De Grandi, and the referee, Pat Henry, have helped to remove ambiguities and make this paper more readable.

Only thanks to the help of many colleagues who allowed us to use unpublished data was it possible to ensure that 92 per cent of the XBACs now have measured redshifts. In particular, we are indebted to Ian Smail who allowed us to use and explicitly quote an unpublished redshift for A 2496 obtained by him and one of us (ACE) at the Las Campanas 100-inch telescope. Two redshifts for southern ACO clusters were obtained by Claudia Mendes de Oliveira and one of us (HE); Claudia's instrumental rôle in the data reduction and her permission to publish the redshifts here are gratefully acknowledged. Usage of five redshifts for ACO clusters in the region around the South Galactic Pole is by kind permission from A.K. Romer and collaborators (1995, private communication). Last but not least we should like to thank Erik Tago and Michael Ledlow for background information on redshifts referred to in the literature.

The identification of non-cluster sources that contaminated the sample we originally started from was greatly facilitated by

the availability of digitized optical images from the POSS and UK Schmidt sky surveys obtained through the SKYVIEW facility. Thanks to Thomas McGlynn, Keith Scollick and co-workers for developing and maintaining SKYVIEW. All of the data analysis presented in this paper was carried out using the Interactive Data Language (IDL). We are indebted to all who contributed to the various IDL User's Libraries; the routines of the IDL Astronomy User's Library (maintained by Wayne Landsman) have been used particularly extensively.

HE and ACE gratefully acknowledge financial support by European Union and PPARC fellowships, respectively. HB thanks the BMFT for financial support from the Verbundforschung programme 50OR93065. JPH acknowledges support by NASA Grant NAGW-201.

Optical observations performed by one of us (JPH) were partially obtained with the Multiple Mirror Telescope, a joint facility of the Smithsonian Institution and the University of Arizona. This research has made use of data obtained through the High Energy Astrophysics Science Archive Research Center Online Service, provided by the NASA-Goddard Space Flight Center, the Leicester Database and Archive Service's XOBSEVER programme, the NASA/IPAC Extragalactic Database (NED), and the SIMBAD database maintained at the Centre de Données Astronomiques de Strasbourg.

## REFERENCES

Abell G.O. 1958, ApJS, 3, 211  
 Abell G.O., Corwin H.G., Olowin R.P. 1989, ApJS, 70, 1 (ACO)  
 Allen S.W., Edge A.C., Fabian A.C., Böhringer H., Crawford C.S., Ebeling H., Johnstone R.M., Taylor T., Schwarz R.A. 1992, MNRAS, 259, 67  
 Andernach H., Tago E., Stengler-Larrea E., 1995, in *The World of Galaxies II*, Astrophys. Lett. & Comm., 31, 27 (updated version)  
 Bade N., Fink H.H., Engels D., Voges W., Hagen H.-J., Wisotzki L., Reimers D., 1995, A&AS, 110, 469  
 Batuski D.J., Burns J.O., Newberry M.V., Hill J.M., Deeg H.-J., Laubscher B.E., Elston R.J. 1991, AJ, 101, 1983  
 Böhringer H. 1994, in *Studying the Universe with Clusters of Galaxies*, Böhringer H. & Schindler S. (eds), MPE report 256  
 Böhringer H., Briel U.G., Schwarz R.A., Voges W., Hartner G., Trümper J. 1994, Nature, 368, 828  
 Bothun G.D. & Schombert J.M. 1990, ApJ, 360, 436  
 Bower R.G., Böhringer H., Briel U.G., Ellis R.S., Castander F.J., Couch W.J. 1994, MNRAS, 268, 345  
 Briel U.G. & Henry J.P. 1993, A&A, 278, 379  
 Brown D.L. & Burns J.O. 1991, AJ, 102, 1917  
 Burg R., Giacconi R., Forman W., Jones C. 1994, ApJ, 422, 37  
 Cappi A., Focardi P., Gregorini L., Vettolani G. 1991, A&AS, 88, 349  
 Capelato H.V., Mazure A., Proust D., Vanderriest C., Lemonnier J.P., Sodré Jr. L. 1991, A&AS, 90, 355  
 Castander F.J., Ellis R.S., Frenk C.S., Dressler A., Gunn J.E. 1994, ApJ, 424, L79  
 Cavaliere A. & Fusco-Femiano R. 1976, A&A, 49, 137  
 Ciardullo R., Ford H., Bartko F., Harms R. 1983, ApJ, 273, 24  
 Collins C.A., Guzzo L., Nichol R.C., Lumsden S.L., 1995, MNRAS, 274, 1071  
 Corwin H.G. 1974, AJ, 79, 1356  
 Couchman H.M.P., McGill C., Olowin R.P. 1989, MNRAS, 239, 513  
 Cristiani S. et al. 1995, A&AS, 112, 347  
 Crawford C.S., Edge A.C., Fabian A.C., Allen S.W., Böhringer H., Ebeling H., McMahon R.G., Voges W. 1995, MNRAS, 274, 75

Crudde R.G., Hasinger G., Trümper J., Schmidt J.H.M.M., Hartner G.D., Rosso C., Snowden S.L. 1991, *Exp. Astr.*, 1, 365

Dalton G.B., Efstathiou G., Maddox S.J., Sutherland W.J., 1994, *MNRAS*, 269, 151

Dalton G.B., Efstathiou G., Maddox S.J., Sutherland W.J. 1994, *MNRAS*, 269, 151

David L.P., Slyz A., Jones C., Forman W., Vrtilek S.D., Arnaud K.A. 1993, *ApJ*, 412, 479

Davis D.S., Bird C.M., Mushotzky R.F., Odewahn S.C. 1995, *ApJ*, 440, 48

De Grandi S. 1996, PhD thesis, Università di Milano

Dickey J.M. & Lockman F.J. 1990, *Ann. Rev. Astron. Astroph.*, 28, 215

Dressler A. & Shectman S.A. 1988, *AJ*, 95, 284

Ebeling H. & Wiedenmann G. 1993, *Phys. Rev. E*, 47, 704

Ebeling H., Voges W., Böhringer H., Edge, A.C. 1993, *A&A*, 275, 360

Ebeling H. 1993, *Abell and ACO Clusters of Galaxies in the ROSAT All-Sky Survey: a Statistical Study*, PhD thesis, MPE report 250

Ebeling H. & Maddox S.J. 1995, *MNRAS*, 275, 1155

Ebeling H., Mendes de Oliveira C., White D.A. 1995, *MNRAS*, 277, 1006

Ebeling H., Allen S.W., Crawford C.S., Edge A.C., Fabian A.C., Böhringer H., Voges W., Huchra J.P. 1996, in *Röntgenstrahlung from the Universe*, H.U. Zimmermann & J. Trümper (eds), MPE Report 263

Edge A.C. & Andernach H. 1995, submitted to *MNRAS*

Edge A.C., Stewart G.C., Fabian A.C., Arnaud K.A. 1990, *MNRAS*, 245, 559

Elbaz D., Arnaud M., Böhringer H. 1995, *A&A*, 293, 337

Ellis R.S. 1983, in *The origin and the evolution of galaxies*, B.T.J. Jones & E.J. Jones (eds), Reidel Dordrecht, p225

Fetisova T. 1982, *Sov. Astron.*, 25, 647

Fetisova T.S., Kuznetsov D.Y., Lipovetskii V.A., Starobinskii A.A., Olovkin R.P., 1993, *Ast. L.*, 19, 198

Fisher J.R. & Tully R.B. 1981, *ApJS*, 47, 139

Galli M., Cappi A., Focardi P., Gregorini L., Vettolani G., 1993, *A&AS*, 101, 259

Giacconi R. & Burg R. 1993, in *Observational Cosmology*, G. Chincarini, A. Iovino, T. Maccacaro, D. Maccagni (eds), ASP Conf. Ser., 51, p342

Gioia I.M., Henry J.P., Maccacaro T., Morris S.L., Stocke J.T., Wolter A. 1990, *ApJ*, 356, L35

Guzzo L. et al. 1995, in *Wide Field Spectroscopy and the Distant Universe*, S.J. Maddox & A. Aragón-Salamanca (eds), World Scientific, p205

Hasinger G., Boese G., Predehl P., Turner T.J., Yusaf R., George I.M., Rohrbach G. 1994, HEASARC LEGACY No. 4, NASA Publication, pp40-56.

Henry J.P., Gioia I.M., Maccacaro T., Morris S.L., Stocke J.T., Wolter A., 1992, *ApJ*, 386, 408

Hoessel J.G., Gunn J.E., Thuan T.X. 1980, *ApJ*, 241, 466

Huchra J.P., Henry J.P., Postman M., Geller M.J. 1990, *ApJ*, 365, 66

Karachentsev I.D. & Kopylov A.I. 1981, *Sov. Astron. Lett.*, 7, 285

Jones C. & Forman W., 1984, 276, 38

Lahav O., Edge A.C., Fabian A.C., Putney A. 1989, *MNRAS*, 238, 881

Lebedev V.S. & Lebedeva I.A. 1991, *Bull. Spec. Ap. Obs. North Caucasus*, 31, 88

Le Borgne J.-F., Mathez G., Mellier Y., Pello R., Sanahuja B., Soucail G. 1991, *A&AS*, 88, 133

Leir A.A. & van den Bergh S. 1977, *ApJS*, 34, 381

Lucey J.R. 1983, *MNRAS*, 204, 33

Lucey J., Currie M., Dickens R. 1986, *MNRAS*, 221, 453

Maza J., Ruiz M.T., Gonzalez L.E., Wischnjewsky M. 1992, *Rev. Mex. Astron. Astrofis.*, 24, 147

McHardy I. 1978, *MNRAS*, 184, 783

Melnick J. & Moles M. 1987, *Rev. Mex. A. and Ap.*, 14, 72

Molendi S. 1995, private communication

Monk A.S., Penston M.V., Pettini M., Blades J.C. 1988, *MNRAS* 234, 193

Mould J.R., Staveley-Smith L., Schommer R.A. et al. 1991, *ApJ*, 383, 467

Muriel H., Nicotra M., Lambas D.G. 1991, *AJ*, 101, 1997

Nichol R.C., Briel U.G., Henry J.P. 1994, *MNRAS*, 267, 771

Oegerle W.R. & Hill J.M. 1992, *AJ*, 104, 2078

Oegerle W.R., Fitchett M.J., Hill J.M. 1991, *ApJ*, 376, 46

Owen F.N., Ledlow M.J., Keel W.C., 1995, *AJ*, 109, 14

Peacock J.A. & West M.J. 1992, *MNRAS*, 259, 494

Pfeffermann E. et al. 1986, *Proc. SPIE*, Vol. 733 (eds Koch, Schmahl), p519

Piccinotti G., Mushotzky R.F., Boldt E.A., Holt S.S., Marshall F.E., Slemitsos P.J., Shafer R.A. 1982, *ApJ*, 253, 485

Pierre M., Böhringer H., Ebeling H., Voges W., Schuecker P., Crudde R., MacGillivray H. 1994, *A&A*, 290, 725

Postman M., Huchra J.P., Geller M.J., Henry J.P., 1985, *AJ*, 90, 1400

Postman M. & Lauer T.R. 1995, *ApJ*, 440, 28

Quintana H., Melnick J., Infante L., Thomas B. 1985, *AJ*, 90, 410

Quintana H. & Ramirez A. 1995, *ApJS*, 96, 343

Raychaudhury S., Fabian A.C., Edge A.C., Jones C., Forman W., 1991, *MNRAS*, 248, 101

Rhee G. & Katgert P. 1988, *A&AS*, 72, 243

Romer A.K., Collins C.A., Böhringer H., Crudde R.G., Ebeling H., MacGillivray H.T., Voges W. 1994, *Nature* 372, 75

Sarazin C.L., Rood H.J., Struble M.F. 1982, *A&A*, 108, L7

Scaramella R., Zamorani G., Vettolani G., Chincarini G. 1991, *AJ*, 101, 342

Schneider D.P., Gunn J.E., Hoessel J.G. 1983, *ApJ*, 264, 337

Schwartz D.A. 1978, *ApJ*, 220, 8

Scott E.L. 1957, *AJ*, 62, 248

Shectman S.A. 1985, *ApJS*, 57, 77

Stark A.A., Gammie C.F., Wilson R.W., Bally J., Linke R.A., Heiles C., Hurwitz M., 1992 *ApJS*, 79, 77

Stocke J.T., Morris S.L., Gioia I.M., Maccacaro T., Schild R., Wolter A., Fleming T.A., Henry J.P. 1991, *ApJS*, 76, 813

Struble M.F. & Rood H.J. 1987, *ApJS*, 63, 543

Struble M.F. & Rood H.J. 1991, *ApJ*, 374, 395

Sutherland W.J. 1988, *MNRAS*, 234, 159

Teague P.F., Carter D., Gray P.M. 1990, *ApJS*, 72, 715

Trümper J., 1993, *Science*, 260, 1769

Vettolani G., Chincarini G., Scaramella R., Zamorani G. 1990, *AJ*, 99, 1709

Voges W. 1992, *Proceedings of Satellite Symposium 3, ESA ISY-3*, p9

Voges W. et al. 1992, *Proceedings of Satellite Symposium 3, ESA ISY-3*, p223

White D.A. 1996, submitted to *MNRAS*

Zabludoff A.I., Huchra J.P., Geller M.J. 1990, *ApJS*, 74, 1

Zwicky F., Herzog E., Wild P., Karpowicz M., Kowal, C.T. 1961–1968, *Catalogue of galaxies and cluster galaxies*, Vols. 1–6